Science Advances
AAAS

Supplementary Materials for

Earth beyond six of nine planetary boundaries

Katherine Richardson *et al.*

Corresponding author: Katherine Richardson, kari@sund.ku.dk

Sci. Adv. **9**, eadh2458 (2023)
DOI: 10.1126/sciadv.adh2458

This PDF file includes:

Supplementary Information
Figs. S1 to S9
Tables S1 to S3
References

Supplementary Information

Reference baseline: Central to the planetary boundaries framework is a comparison of the state of the individual boundary processes to Holocene conditions. In referring to the Holocene, we use its geological definition, as the latest warm inter-glacial Epoch of the Quaternary Period (covering the last 3 million years) of the Earth system. Technically, the Holocene covers the last 11,700 years of Earth's history and extends to the present. For the purposes of this study, however, we refer to Holocene conditions as those the Earth experienced from 11,700 years ago until 0 BCE or 1700, depending on the analysis. This pre-industrial period in Earth history constituted an extraordinarily stable state of the Earth system, with a climate system oscillating only 0.5 °C from the pre-industrial global mean surface temperature (*9*). During the whole of the Pleistocene epoch (from 2.6 million years ago), the Earth system has oscillated between long glacial periods followed by shorter inter-glacial intervals, with a number of inter-glacial periods identified in just the last one million years, of which the last is the Holocene) (*19, 98*). Earth system modelling and ice-core data show that the Earth system never reached a change of 2°C of global mean surface temperature during all these warm inter-glacials (*99*), providing evidence of the Earth system's capacity to remain within inter-glacial conditions, to a certain degree even outside of the Holocene range, if Earth system interactions and feedbacks are kept intact. "Holocene-like" is then used in the text to refer to an Earth system that may be outside of the Holocene maximum range of variability for Earth system regulating processes and systems (planetary boundaries) but still remains in an inter-glacial state, i.e., has not crossed thresholds that irreversibly move the Earth system away from Pleistocene inter-glacial conditions (e.g., > 2°C increase of global mean surface temperature). The reference point for a safe operating space of the Planetary Boundaries, is thus to maintain the Earth system in a manageable inter-glacial Holocene-like state.

Boundary updates:

Biosphere Integrity:

Genetic diversity within species facilitates adaptation and evolutionary change under changing environments (*100,101*) and promotes the resilience, productivity, and functionality of both marine and terrestrial ecosystems (*102,103*). However, implementing a control variable for genetic diversity in the Planetary Boundaries framework has been hampered both by lack of data, adequate predictive methods and of a consensus on what are the most relevant genetic metrics. The recent accumulation of genetic data across thousands of species from the poles to the tropics, the revolution of whole-genomic sequencing and the inception of new approaches, i.e., macrogenetics (*104-108*) pave the road for capturing the global genetic variability and its changes over time. Currently, knowledge of the global geography and the temporal trends of intra-specific diversity is still limited for many taxa across the tree of life (*104,106*) and methods to predict future changes are still in development. Ideally, however, within a decade we should be in the position to estimate across hundreds of species losses in haplotypes, heterozygosity, functional genomic diversity or mutation load and predicting future changes using Mutation-Area Relationships MARs (*23*) for capturing globally extinction dynamics below species level (*109*) and therefore surpass the inability of species-level extinction estimates to capture on-going rates of biodiversity loss.

Biosphere function: Functional integrity of the biosphere is provisionally (i.e., until a more comprehensive metric of the functional influence of the biosphere on the state of the planet is available) measured by the human appropriation of net primary production, HANPP (*cf. 32*) in comparison to the Holocene value and variation of NPP. NPP is used as a proxy for the energy available to the biosphere to support its growth, maintenance, differentiation, and networking. HANPP includes both NPP altered (largely: reduced or eliminated) by human activity or harvested (minus backflows).

The value and the variation of NPP during the pre-industrial Holocene was computed as follows. A 130,000-year climate simulation of the last glacial cycle, including the Holocene, was conducted with Climber-2, an Earth system model of intermediate complexity (*110*). The time step of the simulation was 100 years and atmospheric CO_2 concentration prescribed. This climate data set was applied to drive the biogeochemical global dynamic vegetation model LPJmL4 (*95,111*) to compute the evolution of terrestrial biome distributions, carbon and water cycle. Values of NPP were analyzed for the period 10,000 to 0 BCE, covering the bulk of the stable pre-industrial Holocene, by statistically combining the 100-year climate inputs with annual variation taken from historical CRU TS 3.23 climatology (*112,113*), as realistic vegetation simulation requires natural variability of climate. For evaluation, however, the resulting annual values of Holocene NPP were subsequently once more averaged for each century to produce a mean NPP on the time scale of a century, removing the annual variation of climate applied. A histogram of the resulting century-scale Holocene NPPs was derived as well as the mean, median and standard deviation (the histogram approximates a bell-shape form, Fig. S1).

Performance of the Climber-2 climate simulation for the Holocene was evaluated by comparing the histogram of temperature variations with the reconstructions (*9,114*). While Kaufman et al. (*114*) combine both marine and terrestrial temperature proxies, albeit with some gaps in geographic coverage, Osman et al. (*9*) combine only marine proxies with the dynamic properties of a climate model to derive estimates of climate. While the Kaufman study (*114*) produces slightly declining global mean temperatures after the middle of the Holocene, the study by Osman et al. (*9*) shows quite constant temperatures with no decline in that period. These authors attribute the decline seen in Kaufman et al. (*114*) and previous estimates to the method used for deriving global temperatures from the proxies and not their climate model. The Climber-2 simulations agree in the evolution of temperature very well with the findings of Osman et al. (*9*), showing a climatically very stable Holocene after the initial transition phase. The temperature histograms show that the Climber-2 simulations and both reconstructions have a very similar variation of temperatures occurring over the Holocene. Note, however, that the reference period for these data sets is different; therefore, the absolute values of the histogram means cannot be directly compared. The figure shows these histograms (left) and the histogram of NPPs from the Climber-2 simulation as applied to the LPJmL biosphere model (right), also showing the relationship between histograms of annual NPPs (but with modern variability), and the century-mean NPPs used for subsequent analysis. Holocene mean NPP was estimated from the modelling to have been 55.9 GtC yr^{-1}, the median 55.8 GtC yr^{-1}, and the formal 1σ-standard deviation 0.54 GtC yr^{-1}.

Historical simulations of NPP*:* The LPJmL4 biosphere model is a well-established, documented, and evaluated dynamic global model of terrestrial biogeochemistry and vegetation structure that is widely used. It allows simulation of vegetation and soil carbon and water fluxes for both natural and fractional agricultural areas at a spatial resolution of 0.5 degrees, amounting to nearly 60,000 pixels to cover the relevant global land surface. See

Schaphoff et al. studies (*95,111*) for details of model structure, process representations and benchmarking.

Daily computations are processed to generate annual output for the simulations used here. A 20,000-year spin-up for the carbon pools produced by natural vegetation is followed by the 130,000-year simulation of the last glacial cycle; a 3000-year spin-up is followed for the historical simulations by a spin-up introducing land use patterns from 1500. The simulation then follows dynamic expansion of land use from 1700 to the present using concurrent values of atmospheric CO_2 concentration. However, climate for the years 1700-1900 is a statistical sample of the period 1901-1930. After 1901, the simulation uses observed CRU climatology, actual land use and atmospheric CO_2 concentrations until 2009. Evaluations are therefore restricted to the time from 1900, except for an estimate of NPP for 1700. Simulations were performed for potential natural vegetation (without any land use), for actual land use, and for keeping atmospheric CO_2 concentration constant at the pre-industrial value in order to separate the direct effects of CO_2 fertilization. Resulting annual NPP was averaged over a 30-year period and the resulting smooth evolution fitted for interpolation and producing an estimate for the year 2020.

HANPP: Quantitative evaluations of human appropriation of NPP (HANPP) are scarce in the literature and vary due to differences in definition, detail, and data used. A review of approaches and findings is given in Haberl et al. (*32*). Fig. S2 illustrates the authoritative definition of HANPP used here. The most detailed and systematic derivation is found in Haberl et al. (*115*) for the year 2000, and a subsequent evaluation for the 20th century in Krausmann et al. (*33*). Although these were derived from baseline NPP simulations for potential natural vegetation also produced by the LPJmL model (from which human appropriation was deduced using a variety of data bases of human land use in a number of relevant categories, corrected for backflows and fires), the model version used then was not the same as the more advanced version of LPJmL used here. We therefore applied the values of HANPP as a percentage of potential natural NPP (*33*) to the potential natural NPP values of the LPJmL simulations used here to derive absolute values of HANPP for selected years. As these displayed a very smooth evolution, they were fitted to derive intermediate values and an estimate for the year 2020.

Evaluation: Fig. S3 and Table S1 present an overview of key NPP results from the biosphere model simulations and corresponding HANPP values. The position of the (provisional) planetary boundary component for functional Biosphere Integrity is marked at 10% and the upper end of the zone of increasing risk at 20% of the pre-industrial Holocene mean value of terrestrial NPP.

Climate Change:

Climate Change control variables of atmospheric CO_2 concentration and total effective anthropogenic radiative forcing and their boundary levels are retained (*1,2*). The planetary boundary for atmospheric CO_2 concentration is set at 350 ppm and for radiative forcing at 1 W m^{-2}. The upper end of the zone of increasing risk is set at 450 ppm for atmospheric CO_2 concentration and at 1.5 W m^{-2} for radiative forcing (*2*). The control variable of radiative forcing describes the aggregate most important anthropogenic impact on the Earth's energy balance via release of greenhouse gases, aerosols, and albedo forcing (*17*), while the control variable of atmospheric CO_2 concentration highlights the currently dominant role and policy relevance of this greenhouse gas. The boundary value for total effective anthropogenic radiative forcing of 1 W m^{-2} is chosen such that it corresponds to the radiative forcing contribution of atmospheric CO_2 alone at its boundary value of 350 ppm (that was reached between 1987—1988), when the positive and negative contributions of other greenhouse gases, aerosols and land-use changes had approximately cancelled out (*17*).

Ozone Depletion

Transgression and current ozone values were estimated from daily measurements from NOAA (*96*) for both hemispheres. These data were spatially aggregated into global monthly medians. In order to compensate for the high annual fluctuations, the current value was calculated as a five-year median for 2016 - 2021.

Freshwater Change

Freshwater supports terrestrial and aquatic ecosystems, mediates flows of material and energy, and regulates the Earth's climate. Thus, it is tightly coupled with the core boundaries of Climate Change, Biosphere Integrity and Novel Entities, as well as the Land-System Change and Biogeochemical Flows boundaries (*14,22*). While the PBs for Novel Entities and Biogeochemical Flows implicitly incorporate quality aspects of freshwater, the Freshwater Change PB explicitly addresses the quantity of freshwater. Terrestrial and freshwater ecosystems have generally adapted to specific quantities of freshwater, which vary naturally both within and between years. The level of wetness of landscapes also regulates climate from micro- to regional and global scales, such that changes in wetness of one location can impact rainfall and consequently river flows and soil moisture both locally and in distant locations (*116-118*).

The earlier PB for Freshwater use explicitly accounted only for human consumptive use of blue water (i.e., from rivers, lakes, reservoirs, and renewable groundwater stores) as a proxy for water cycle change over land, with minimum levels of streamflow requirements in aquatic ecosystems as a sub-global boundary condition (*2,119*). This control variable misses – or aggregates too broadly – various important anthropogenic disruptions to the hydro-ecological and hydro-climatic Earth system functions of freshwater, such as land-use, land management and climate change impacts on soil moisture, evaporation and precipitation (*116,120,121*), and dam operation impacts on temporal variability of streamflow (*122*). The new approach chosen here better acknowledges the many Earth system impacts that freshwater changes have beyond aquatic ecosystem integrity on, for example, terrestrial productivity, biome resilience (*123*), carbon and nutrient transport, uptake, and storage (*124,125*), as well as regional atmospheric circulation (*126*) by accounting for changes in both green water (soil moisture) and blue water (streamflow). Both local and global limits for freshwater change are based on variability within the anthropogenically relatively undisturbed pre-industrial period (used as proxy for Holocene conditions), such that persistent and widespread exceedance of these bounds represents a shift in the freshwater cycle.

Boundary value and current states of the Freshwater Change boundary were derived by analyzing spatially and temporally explicit streamflow (blue water) and root-zone soil moisture (green water) data from the inter-model comparison project ISIMIP 2b (*127*). For root-zone soil moisture, data from four global hydrological models (GHMs) were used: CLM50, LPJmL, MPI-HM, and PCR-GLOBWB. Streamflow data were derived from six GHMs: H08, LPJmL, MATSIRO, MPI-HM, PCR-GLOBWB and WaterGAP2. Each GHM was forced with modelled climate from four different general circulation models: GFDL-

ESM2M, HadGEM2-ES, IPSL-CM5A-LR and MIROC5; with the exception of MPI-HM lacking HadGEM2-ES. This resulted in 15 ensemble members for root-zone soil moisture and 23 for streamflow.

The control variables were calculated as follows, for green and blue water separately

1. The local baseline range was set by determining dry (5th percentile) and wet (95th percentile) bounds during the pre-industrial (1661–1860) period, for each month of the year, for each 30x30 arcmin grid cell and for each ensemble member. Values outside of these bounds are referred to as “local deviations”.
2. For each month and each ensemble member, the percentage of global ice-free land area with local blue/green water deviations, both for dry and wet deviations, was calculated by aggregating the areas of grid cells with local deviations. Areas with dry and wet deviations were summed to derive total area with deviations.
3. For each year and ensemble member, the mean of monthly areas with deviations was used to calculate the percentage of annual global ice-free land area with local blue/green water deviations.
4. For each year, the median of ensemble members’ values was taken.

These analyses result in a time series of annual global land area with streamflow/root-zone soil moisture deviations, starting from the pre-industrial period (1661–1860) and continuing to the industrial period (1861–2005). The end date is limited by the ISIMIP 2b simulation protocol, due to lack of reliable estimates on some of the major anthropogenic forcings, such as irrigation extent (*128*), at the appropriate scales. Global trends in many of the key drivers, such as irrigation area (*84*), water use (*129*), dam construction (*130*) and forest loss (*131*) have increased since 2005. Consequently, the “current’’ estimate (mean of 1996–2005) presented here is likely conservative.

The annual global land area with local deviations during the pre-industrial period is used to define the global boundary condition. The global land area with local blue and green water deviations was relatively stable during this period, varying approximately within 1.5 percentage points around the median of 9.4% (blue) and 9.8% (green). The global boundary is provisionally set at the upper limit (95th percentile) of this pre-industrial variability, which was 10.2% for blue water and 11.1% for green water. This precautionary placement was chosen because scientific evidence of the levels of blue and green water deviations that may trigger irreversible changes in Earth system functions is currently lacking. To acknowledge uncertainties related to both data and the exact boundary position, the upper limit of the zone of increasing risk is provisionally set at 50% of land area with freshwater deviations, for both blue and green water, following the reasoning by Barnosky et al. (*132*). At the landscape scale, undisturbed patches are prone to tip into a new state when 50-90% of surrounding patches are disturbed. Given the interacting and multiplying effects at larger scales, shifts in 50% (or less) of the Earth’s ecosystems can be expected to trigger global forcings and rapid changes in remaining systems (*132*).

Currently (mean of years 1996–2005), about 18.2% (blue) and 15.8% (green) of the global land area experience local freshwater deviations, which we interpret as a substantial exceedance of the Freshwater Change boundary, given the very narrow variability in the pre-industrial period. The blue water boundary was transgressed in 1905, and the green water boundary in 1929 (*46*). Even the ensemble interquartile ranges surpass the boundaries in the latter half of the 20th century, which increases confidence on our conclusion that the boundary is transgressed but also underlines the uncertainty on the exact timing and magnitude of transgression (*46*). Transgressing the Freshwater Change boundary is consistent with 'the great acceleration' (*2*) of anthropogenic drivers impacting freshwater. Our estimates of an increase in freshwater deviations are in good agreement with results from many other studies of changes in the global water cycle. These include increases in precipitation (*133*) and river flow (*134*) extremes, increases in drought occurrence and severity (*135*), intensification of the water cycle (*136*), widespread and severe violations of environmental flows (*136-139*) of river flow regimes (*122*). The geographic patterns identified in our assessment also agree well with previously reported research, where tropics and subtropics show the greatest drying and the northern latitudes the greatest wetting (*46,140*).

The conclusion that human activities have brought the Freshwater Change planetary boundary into a zone of increasing risk of changing Earth system state is consistent with many reported freshwater-mediated impacts. For blue water, perhaps the most dramatic example of a link to Earth system processes is the destruction of the Aral Sea, which occurred due to substantial streamflow reductions from overuse of water for irrigation, and resulted in lake depletion with consequent ecological degradation and regional climate change (*141*). Green water changes have been associated with productivity loss in both natural and cultivated lands, as exemplified by drying-induced forest dieback in all continents (*142*) and increases in flood and drought-induced food production shocks, particularly in South and East Asia, Australia, and North Africa (*143*). Examples of ecological and climatic impacts of water surpluses are habitat loss in the Central Amazon floodplains due to anthropogenic flood pulse disturbance (*144*), and increased greenhouse gas emissions from reservoirs (*145*), both created by dam construction and operation. Reversing the Freshwater change PB transgressions will likely require reduced human disturbance through land-use and land management, water withdrawals, large water transfers, reservoirs and dam operations, and greenhouse gas and aerosol emissions. Note, however, if the previously defined boundary (*1,2*) were applied, human impacts on this boundary would still be considered as being within the safe operating space (*49*).

Aerosol Loading

The atmospheric burden of small particles (aerosols) have both physical and biogeochemical effects in the Earth system. They influence Earth's energy balance by absorbing and scattering of radiation, and changing cloud properties (*17*). These physical effects are represented in the climate change planetary boundary, but there are also other complex interactions between aerosols, climate and the biosphere. One example is the dimming effect of aerosols, i.e., a higher aerosol loading leads to less surface irradiance, which can cause for instance a relative reduction in surface warming and evaporation. Aerosols further affect the hydrological cycle by influencing clouds and precipitation (*146*), although these are yet to be fully understood. Moreover, aerosols influence primary production, human and organism health, and ecosystem function, e.g., through the deposition or inhalation of trace substances, and altering the direct irradiance that affects photosynthesis.

Aerosol information is here based on the data assessment by (*57*). We calculate the area-weighted hemispheric difference ($\overline{\Delta\tau}$) in the aerosol optical depth (τ) for present-day. τ is a measure of the aerosol extinction, i.e., scattering and absorption of irradiance. For being close to observations, we use all twelve τ datasets from satellites, re-analysis, and climatologies in the time period 1998-2020 that are listed in Table 1 of (*57*). We first calculate for each data set $\Delta\tau = \tau(\phi) - \tau(-\phi)$ at each latitude (ϕ) between 60 degrees North and 60 degrees South. We than compute the average over all latitudes weighted by the latitude-dependent area. The reported values for $\overline{\Delta\tau}$ are the mean across all datasets and the data-to-data standard deviation as uncertainty measure. We assume that aerosol impacts scale with $\overline{\Delta\tau}$. Given that monsoon dynamics and the associated regional rainfalls respond to changes in anthropogenic aerosols *(147-150),* we assume the effects of anthropogenic aerosol release mimic reseale from natural sources.

Ocean Acidification

The current (i.e., year 2022) global averaged saturation state of aragonite (Ω=2.8) is estimated from the climatological average value of 3.03 in year 2000 and the corresponding global decrease of 0.1 per decade (*71*). This corresponds to an estimated decrease of 0.64, or 81%, of the pre-industrial value of 3.44 (*2).*

Land System Change

This update retains the same general approach used earlier (*2*). However, improved methodology is available for estimating the remaining area of forest. These improvements include major advancements in satellite image technology and improved classification algorithms, which formerly relied on statistical methods but have now shifted towards using machine learning approaches.

Global*:* The global boundary is defined as the area of forested land (on the ice-free land surface) that is maintained, expressed as a percentage of the potential area of forested land in the Holocene (that is, the area of forest remaining assuming no human land-cover change). The boundary of 75% of potential forest cover remaining is retained. The boundary has been constructed as a weighted aggregate of the three individual biome boundaries as described below.

Biome: Boundaries for each forest biome are defined as the forest area maintained in each of the three major forest biomes – tropical, temperate, boreal – expressed as a percentage of the potential forest area in each of these three biomes. The estimated boundary for each of the biomes is based on (i) the relative potential of land-cover change within each biome to influence the climate system at the global level, and for some biomes, (ii) the potential for a threshold of land-cover change beyond which self-reinforcing feedbacks within the biome lead to land-cover change across a much larger area. This approach is identical to the one used in 2015.

The boundary levels and current status of the eight major forest biomes are given in Table 1. Seven of the eight biome-level boundaries have now been transgressed, one more than in the 2015 assessment. In addition, there have been some notable shifts in the amounts and patterns of deforestation:

Tropical forest. The boundary is retained at 85% of potential forest cover to be maintained, based on the potential for a threshold of land-cover change in the Amazon Basin tropical forest beyond which much of the forest is converted to a savanna or grassland. The mechanism for such a transition, described in more detail (*2*) but is based on the reduction of evapotranspiration as the tropical forest is converted into grazing or cropping land, and the subsequent decrease in rainfall across the basin.

Temperate Forest. There has been no change in the overall pattern of deforestation of temperate forests compared to the 2015 assessment (*2*). Both European and Asian forests remain in a transgressed state, while North American temperate forests are still within the safe operating space. However, the areas of both the North American and European temperate forests appear to be considerably reduced. The Asian temperate forest, on the other hand, has increased in area from since 2015. While changes in the methodology used to estimate forest cover may explain some of these differences, the some of the increase in forest cover in Asia may be due to the very large reforestation initiative in China.

Boreal forest. Both the North American and Eurasian boreal forests have decreased very slightly in area since 2015. Given the changes in methodology, these estimated increases in boreal forest cover are not likely to be significant. The current areas of both boreal forests indicate substantial transgression of this boundary.

Earth system effects of differing scenarios of transgression of Land System Change and Climate Boundaries

We apply ESM CM2Mc-LPJmL (a configuration of the Potsdam Earth Model POEM (*85*), which includes marine (BLING) and terrestrial (LPJmL5) biosphere models, to explore short- and long-term biosphere responses to climate change. Especially the model's advanced terrestrial biosphere is able to account for important biological processes such as competition between vegetation functional types, tissue mortality, fire dynamics and water stress that influence the land carbon balance and biophysical feedbacks on climate.

Development of terrestrial biologically mediated C-sinks:

CM2Mc-LPJmL v1.0 (*85*) is a coupled Earth system model, combining the coarse-grained but relatively fast atmosphere and ocean model CM2Mc (*151*) with the state-of-the-art dynamic global vegetation model (DGVM) LPJmL5 (*95,111,,152*). CM2Mc is a coarse (3°x3.75° latitude-longitude) configuration of the Climate Model CM2 (*153*), developed at the Geophysical Fluid Dynamics Laboratory (GFDL). The original CM2Mc model includes the Modular Ocean Model 5 (MOM5) and the global atmosphere and land models AM2-LM2 or AM2-LM (*154*) with static vegetation. In CM2Mc-LPJmL, the land component LM/LM2 is replaced by the dynamic global vegetation model LPJmL5. AM2 and MOM5 remains dynamically coupled to the model framework. The different model components are connected by the Flexible Modeling System (FMS), developed by GFDL.

LPJmL5 (Lund-Potsdam-Jena managed land) is a state-of-the-art DGVM, which is well established and thoroughly validated (*95,111,152*)). It models water and carbon fluxes for natural and managed land, carbon stocks and the global surface energy balance, but the nitrogen cycle remained deactivated in keeping with previous model setups (*85*). LPJmL5 simulates the impact of bioclimatic limits and effects of heat, productivity, and fire on plant mortality to determine the establishment, growth, competition, and mortality for different plant functional types (PFTs) in natural vegetation and crop functional types (CFTs) on managed land. The model is forced by climate and soil data. New developments since the original publication (*155*) led to the incorporation of a water balance (*156*), agriculture (*157*), wildfire in natural vegetation (*158,159*), and the impact of multiple climate drivers on phenology (*160,161*).

Using LPJmL5, enables the model to make, e.g., use of its advanced land use scheme, the process-based fire model SPITFIRE, a representation of permafrost and a state-of-the-art water cycling. These processes within LPJmL5 have large effects on the location, timing and magnitude of the atmospheric water fluxes and precipitation through plant evapotranspiration, surface temperature and the simulated canopy humidity. The fully coupled energy and water cycle allows to investigate the impact of biophysical atmosphere-biosphere feedbacks on global climate trajectories and to quantify the impacts of deforestation or afforestation scenarios.

Compared to the published version of CM2Mc-LPJmLv1.0 (*85*), the version used in this paper incorporates a few small changes, including setting the net water influx from rivers into the ocean to zero to avoid unrealistic high fluctuations of the sea level. The sea level can still change due to sea ice melt and thermal expansion. We also improved the initialization of the model after starting from a previous state by including more variables in the saved state file. Finally, we slightly adapted the canopy conductance used in the photosynthesis routine to increase plant productivity and better match historic trajectories of the land carbon sink.

Model protocol:

The model experiments of this paper are consistent with Drüke et al. (*85*): After a 5000-year stand-alone LPJmL spin-up, a second fully coupled spin-up under pre-industrial conditions without land use was performed for 1500 model years. In this way, we ensure that the model starts from a consistent equilibrium between the long-term soil carbon pool, vegetation, ocean, and climate.

The subsequent transient historic phase of the model is performed from 1700-2018, using historic land use data from 1700 (*162*) and historic concentrations of greenhouse gases, solar radiation, ozone concentrations and aerosols from 1860, which were kept at pre-industrial conditions beforehand. From 2004 on, only greenhouse gas forcing remains, while aerosols, solar radiation and ozone are set to their corresponding 2003 values. Scenario values for atmospheric CO_2 concentration were set to 350, 450 and 550 ppm, while scenarios for land system change (pattern of remaining forest) were generated by an algorithm that replaces natural forest by managed grassland and crops adjacent to land-use areas until the extent of natural land was reduced to the designated fractions in the different climate zones (tropical, temperate, boreal).

In the following scenario names, climate change is denoted CC and land system change as LSC. The descriptors “PB”, “upper” and “beyond” refer to three levels of forcing of these planetary boundary dimensions. The “planetary boundaries (PB)” setting delineates the safe operating space, i.e. the planetary boundary itself; the “upper” value is at the upper end of the zone of increasing risk, identified based on conditions that while beyond the boundary are still potentially in an interglacial state; and the highest value analyzed (“beyond”) gives a forcing that likely endangers the interglacial condition of Earth.

- PB CC and PB LSC: From 1989 on constant atmospheric CO_2 concentrations at 350 ppm and constant land use pattern from 1989 for 800 years.

- Upper CC and PB LSC: From 2019 for 10 years linear trajectory to 85/50/85 % (tropical/temperate/boreal) remaining natural vegetation and to 450 ppm (1 % yearly increase from 2019 levels). From 2029, constant land use pattern and constant atmospheric CO_2 concentration at 450 ppm for 800 years.
- Upper CC and upper LSC: From 2019 for 10 years, linear trajectory to 60/30/60 % (tropical/temperate/boreal) remaining natural vegetation and to 450 ppm (1 % yearly increase from 2019 levels). From 2029, constant land use pattern and constant atmospheric CO_2 concentration at 450 ppm for 800 years.
- Upper CC and beyond LSC: From 2019 for 10 years, linear trajectory to 40/20/40 % (tropical/temperate/boreal) remaining natural vegetation and to 450 ppm (1 % yearly increase from 2019 levels). From 2029 constant land use pattern and constant atmospheric CO_2 concentration at 450 ppm for 800 years.
- Beyond CC and upper LSC: From 2019 for 34 years, linear trajectory to 60/30/60 % (tropical/temperate/boreal) remaining natural vegetation and to 550 ppm (1 % yearly increase from 2019 levels). From 2053, constant land use pattern and constant atmospheric CO_2 concentration at 550 ppm for 800 years.
- Beyond CC and beyond LSC: From 2019 for 34 years, linear trajectory to 40/20/40 % (tropical/temperate/boreal) remaining natural vegetation and to 550 ppm (1 % yearly increase from 2019 levels). From 2053, constant land use pattern and constant atmospheric CO_2 concentration at 550 ppm for 800 years.

Model Evaluation:

The performance (Fig. S6) of the newly coupled CM2Mc-LPJmL model is similar to CM2Mc-LaD (*140*) and comparable to results from the Coupled Model Intercomparison Project (CMIP5, CMIP6) (*163*). Furthermore, the model shows a stable performance over 750 years and reasonable reactions to climate and land-use change (for details see (*85*)).

Fig. S4 shows the modeled spatial patterns of a10-year average of recent historical surface temperature and precipition, and a comparison of their zonal means with ERA5 reanalysis. Fig. S5 shows the modeled temporal development of the **y**early and decadal global mean temperature anomaly (relative to the reference period 1951–1980) compared to GISTEMP data. Fig. S6 compares the simulated distribution of above-ground biomass against the GlobBiomass data set (*164*).

Model results (Fig. S7, Fig. S8, Fig. S9, Table S2)

The “safe” climate and land system change boundaries were passed around 1990. Atmospheric CO_2 concentration passed 350 ppm and the remaining fraction of natural land area fell below 85/50/85 % of tropical/temperate/boreal forest cover (lower LSC). Today, we are heading to the upper end of the zone of increasing risk for these two boundaries. The “next stop” before entering dangerous territory is therefore the upper end of the zone of increasing risk at 450 ppm and the upper end of the zone of increasing risk for land system change with 60/30/60 % forest cover retained (upper LSC).

To complete the modeling experiments, we also ran experiments maintaining the climate dimension at the upper end of the zone of increasing risk at 450 ppm, while the LSC boundary was maintained (LSC at the planetary boundary) or transgressed to beyond the zone (40/20/40 %, transgressed LSC), and experiments where CC was beyond the zone of increasing risk at 550 ppm and LSC was either at the upper limit of the zone of increasing risk or beyond.

The modeling results provide support for the placement of the Climate Change planetary boundary at 350 ppm, as the temperature increase from pre-industrial would be within ca. 1.3 °C above preindustrial levels, below the Paris target of 1.5 °C and only a small cumulative net amount of carbon (ca. 60 GtC) emitted from the biosphere over the modeling period of 800 years.

At the same time, the long-term change in terrestrial carbon stocks indicates that respecting the planetary boundary for LSC retains a stabilizing influence, i.e., a C sink, on climate when atmospheric CO_2 is 450 ppm, in contrast, an LSC value advanced to the upper edge of the zone of increasing risk produces the opposite, an additional leakage of carbon to the atmosphere, i.e., an acceleration of warming and hence implies further transgression of climate into the dangerous zone. This is even more the case if the upper end of the zone if increasing risk for the land system change boundary is transgressed.

If atmospheric CO_2 concentration were to rise to 550 ppm, i.e., attain a value beyond the zone of increased risk for the Climate Change boundary, not only would an 0.7-0.8 °C of additional long-term warming occur over land compared to the long-term temperature at 450 ppm, but also around 150 GtC of carbon loss would occur from land. The results of the different experiments are summarized in Table S2 and Fig. 2 of the main text.

When transgressing the LSC boundary by expanding managed land in CM2Mc-LPJmL, natural vegetation is partially replaced by pasture and crops. The decrease of biomass and forest cover affect biophysical feedbacks mainly in three distinct ways: 1) Crops transpire less water than large forests, thus decreasing the water flux to the atmosphere and in turn humidity, precipitation, and cooling by latent heat exchange (*165*). 2) Crops and grasses have a higher albedo than a closed forest, therefore impacting the energy cycles towards decreased surface temperature (*166*). 3) Temperatures increase due to a decrease in roughness length (*167*). The net effect of these biophysical feedback mechanisms is a warmer and drier climate in most regions. Specifically in the tropics, latent and sensible heat fluxes far exceeded the potential cooling of an increased surface albedo.

<u>Development of biologically mediated C-sinks in the ocean:</u> Model simulations of carbon fluxes, primary production (PP) and the saturation state of aragonite (Ω) were analyzed in the initial (i.e., from 1988) and final (after ~800 years) 30-year period. In addition, biogenic particulate fluxes were compared with empirically derived estimates calculated from temperature and PP (Table S3). The biological module was based on the BLING model and monthly averaged fields of temperature, biological phosphorous uptake and the sinking flux of particulate phosphate (P) were applied for calculating PP and export fluxes of particulate organic carbon by assuming a molar C:P ratio of 106. New production (NP) and the mesopelagic C-flux (F_{500m}) were calculated from the particulate flux at 100 m and 500 m depth, respectively.

The empirically derived estimate of NP was calculated from sea surface temperature (SST), PP and the export ratio (*ef*) (i.e., $ef = (a+b\ SST)\ PP^c$, where *a*,*b* and *c* are constants (*90*), and compared with simulated NP. Mesopelagic particulate C-flux (F) was estimated from the empirical relationship suggested by (*91*) (i.e., $F(z) = F(z_0)\ (z/z_0)^b$; $F(z_0)$ is the flux at 100 m depth, i.e., NP) where the power dependence of the remineralisation length scale (*b*) decreases linearly with temperature in the upper 500 m ($T_{0\text{-}500m}$). Monthly averaged values of the C-flux at 500 m depth (F_{500m}-E) were calculated from NP and $T_{0\text{-}500m}$.

Sensitivity of C-inventories and biogenic fluxes: SST increased by 1.4 ºC between the 550 and 350-simulation and temperature in the upper 500 m increased correspondingly by 1.1 ºC (Table S3). The total inventory of DIC increased by 946 GtC of which 273 GtC accumulated in the upper 1000 m. The accumulation of DIC was mainly driven by increased atmospheric pCO_2 whereas only a minor fraction could be ascribed to biogenic fluxes. A characteristic response time (e-folding time) for accumulation of total DIC and DIC in the upper 1000 m was estimated (i.e., approximating three e-folding times with the elapsed time until the change in DIC had reached 95% of its final change) for the 550-simulation to be 261 and 155 years, respectively. Both the 450 and 550 ppm simulations showed a continuous rise in DIC_{tot} during the entire 800-year period.

New production decreased by ~4 % between the two experiments (550 and 350) whereas the decreased mesopelagic flux at 500 m depth of 0.08 and 0.19 GtC yr^{-1} for the model and empirically derived fluxes, respectively, implied a significant reduction of 5-15% of the organic matter flux to the ocean interior. A small increase of NP between the 1988 and 350-experiment (in both the model and empirically derived NP) could be explained by the slight increase in PP (e.g., 51.3 GtC yr^{-1}) in the end of the 350-experiment. Model- and empirical estimates of NP and F_{500m} were generally in good accordance.

Saturation state of aragonite: The initial Ω in the model (i.e., calculated from the carbonate system and based on SST, surface salinity, DIC and alkalinity) was in general accordance with climatology, i.e., the simulated value of 3.2 in 1988 is within 0.05 of the estimated climatological value (Table S3). The final state in the 550 ppm simulation (Ω=2.51) crosses the planetary boundary (80% of the pre-industrial value corresponding to Ω=2.75). A characteristic response time was estimated (see above) and the 450 and 550-simulations were characterized by a decadal decrease of 0.1, in accordance with the current climatological change (*71*). Thus, the major change in surface Ω occurs within a few decades.

Fig. S1. Histograms comparing the variation of temperature during the pre-industrial Holocene (10.000-0 BCE) for two reconstructions and the Climber-2 climate model simulation (left; note that the reference period for each period is different, so that the shape of the histograms can be compared but not the values of the anomalies plotted), and of the century-mean and annual (with modern climate variability) NPPs simulated with the LPJmL biosphere model (right).

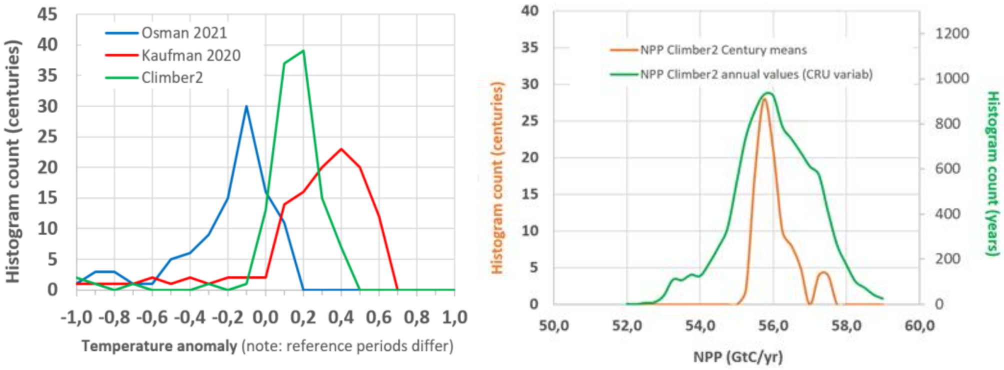

Fig. S2. Schematic of the definition of HANPP used in this study (not to scale; following the definitions of (*75*)).

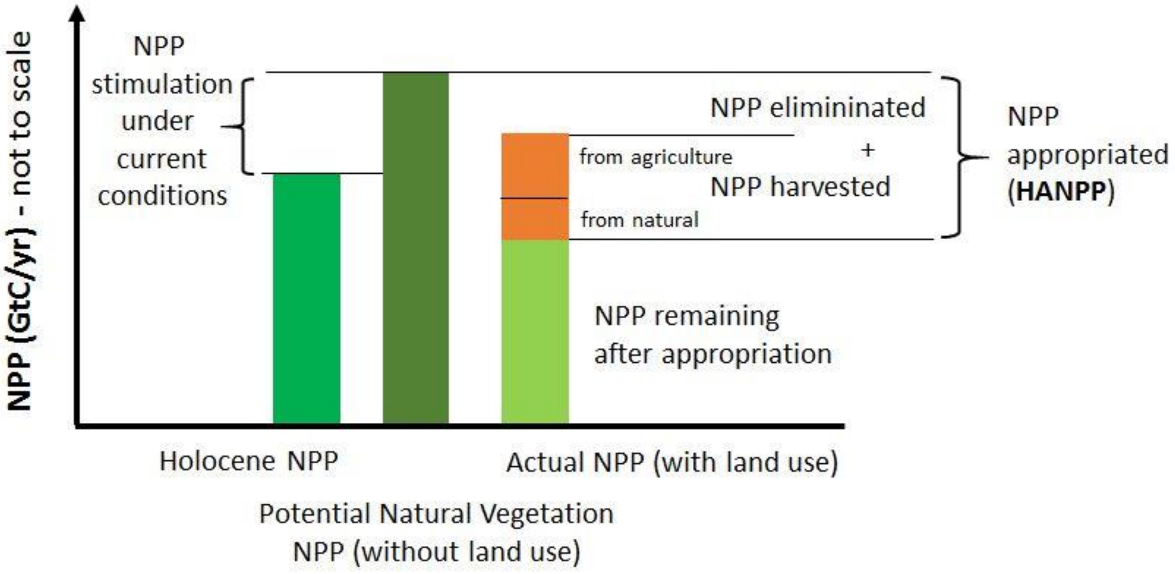

Fig. S3. Summary of key NPP and HANPP results from the LPJmL4 biosphere model simulations.

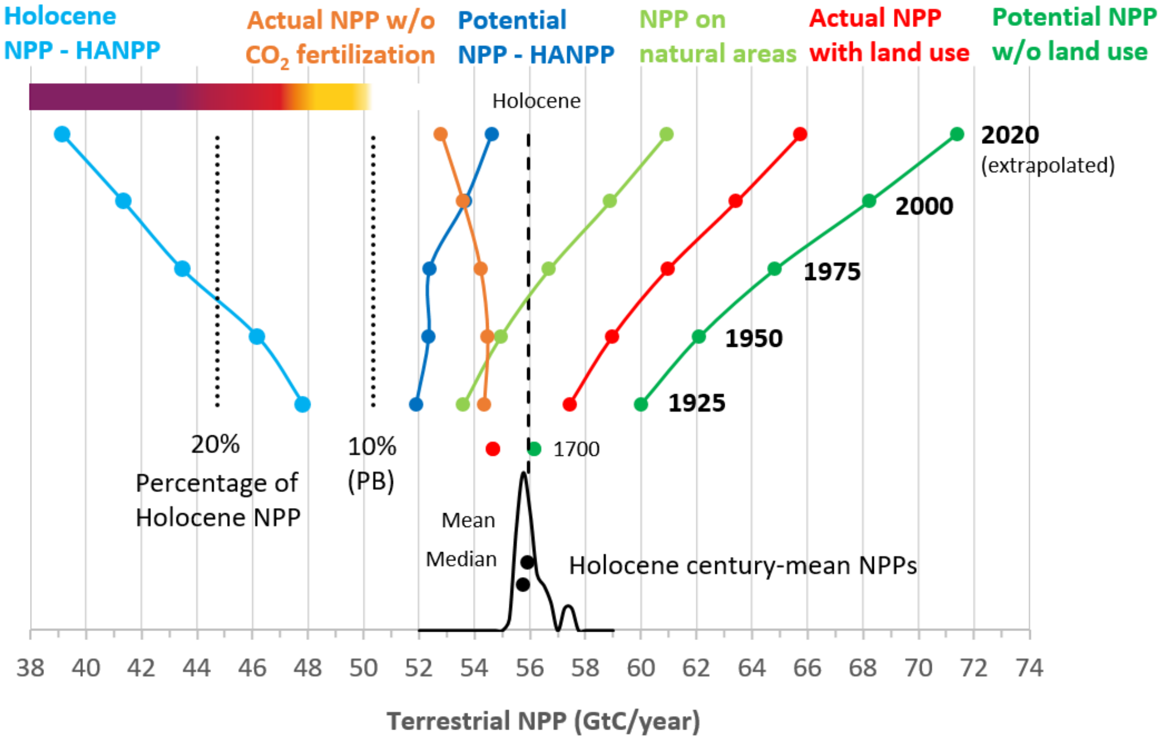

Fig. S4. (a) Global surface temperature from CM2Mc-LPJmL averaged over the period 1994–2003, (b) global precipitation from CM2Mc-LPJmL averaged over the period 1994–2003, (c) zonal mean temperature from CM2Mc-LPJmL (red line) and ERA5 data (blue line) averaged over the period 1994–2003, (d) zonal mean temperature from CM2Mc-LPJmL (red line) and ERA5 data (blue line) averaged over the period 1994–2003. Plot is analogous to (*85*).

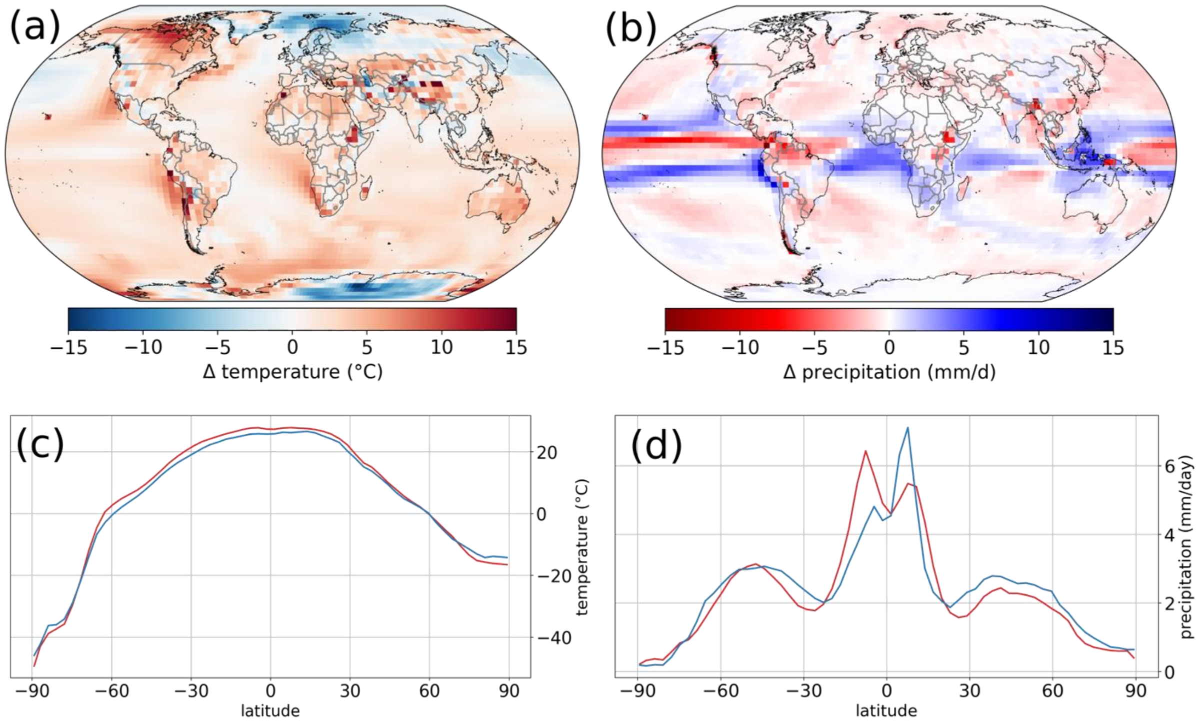

Fig. S5. Yearly and decadal global mean temperature anomaly (relative to the reference period 1951–1980) of CM2Mc-LPJmL compared to GISTEMP data from 1880–2018. Note that, from 2004 on, only greenhouse gas forcing remains, while aerosols, solar radiation and ozone are set to their corresponding 2003 values. Plot is analogous to (*85*).

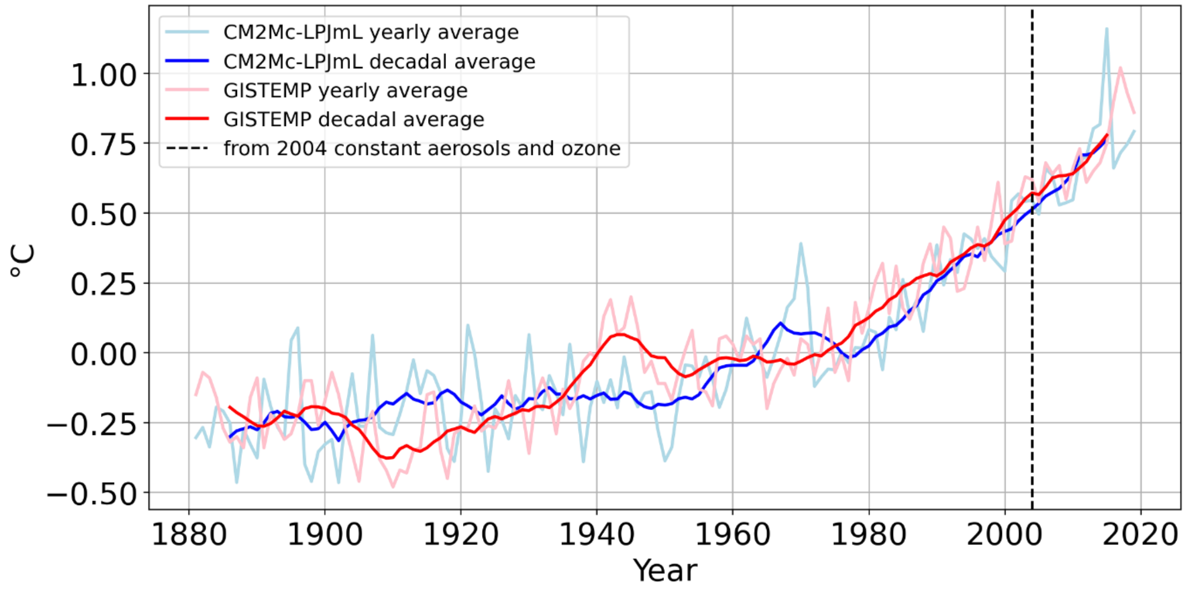

Fig. S6. (a) Mean global above-ground biomass of GlobBiomass (*198*) evaluation data. (b) Mean global above-ground biomass of CM2Mc-LPJmL over the period 2006-2015. (c) Difference of the above-ground biomass between CM2Mc-LPJmL and GlobBiomass evaluation data. Blue/red colors denote an overestimation/underestimation of biomass by CM2Mc-LPJmL. (d) Latitudinal sum of above-ground biomass from CM2Mc-LPJmL (blue line, R2=0.65, NME=0.58) and GlobBiomass evaluation data (red line). Plot is analogous to (*85*).

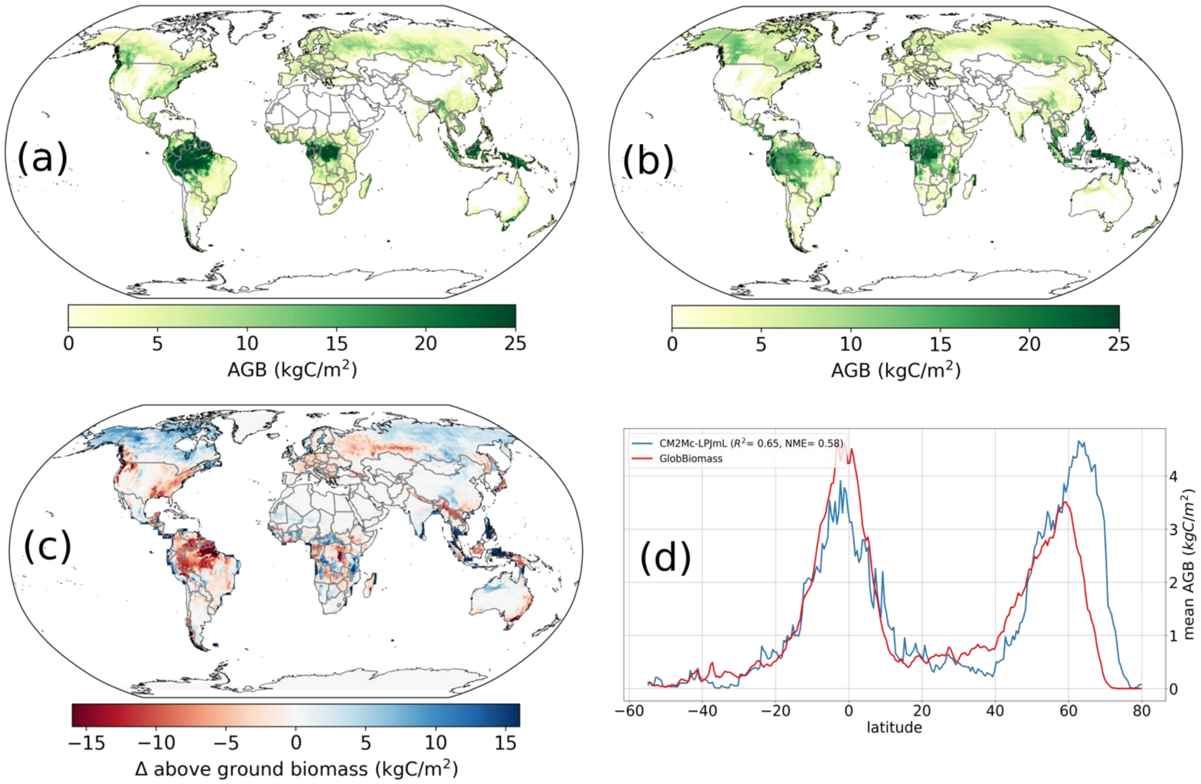

Fig. S7. (a) Total land carbon, (b) vegetation carbon, (c) soil carbon and (d) litter carbon for the different experiments, including the historic period until 2019 in black. In the first 100 years of the scenarios, the fertilization effect leads to a strong increase in total land carbon for the experiments at 450 ppm/lower LUC and 550 ppm/upper LUC, respectively. Soil carbon in the other experiments decreases due to increased heat stress and increased LUC.

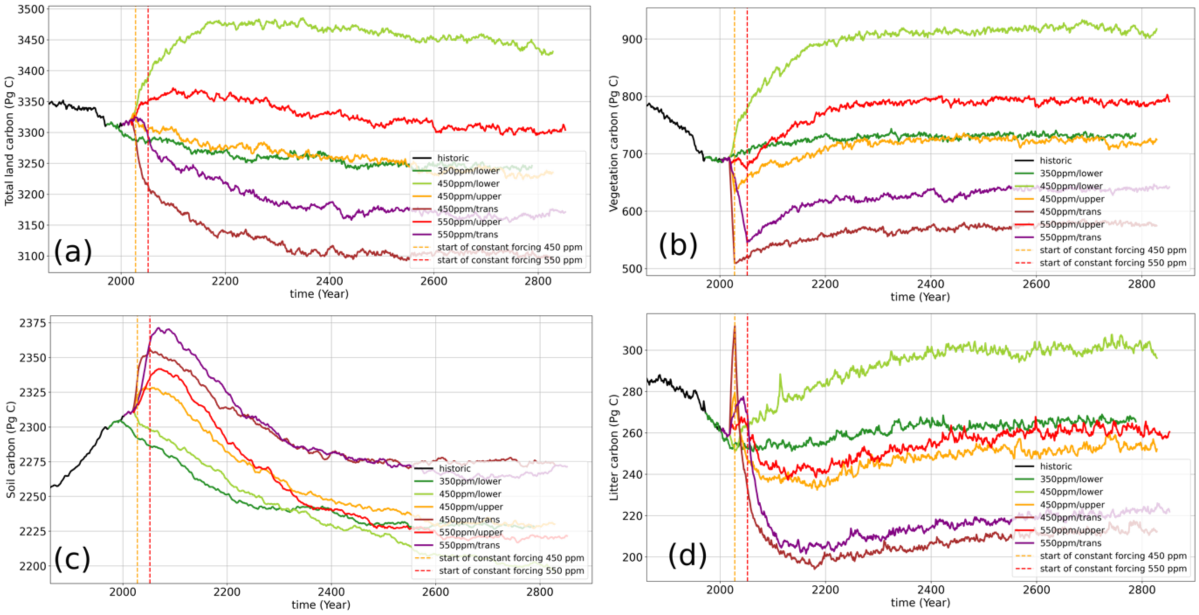

Fig. S8. Global mean land temperature in a 30-year running mean for the different experiments, including the historic period until 2019 in black. Temperature increases mainly due to increasing atmospheric CO_2 concentrations and to a lesser extent due to biophysical feedbacks for the different land use change scenarios. Long-term temperature increase is due to lag effect of heat transfer in the ocean and to a lesser extent in the different soil layers.

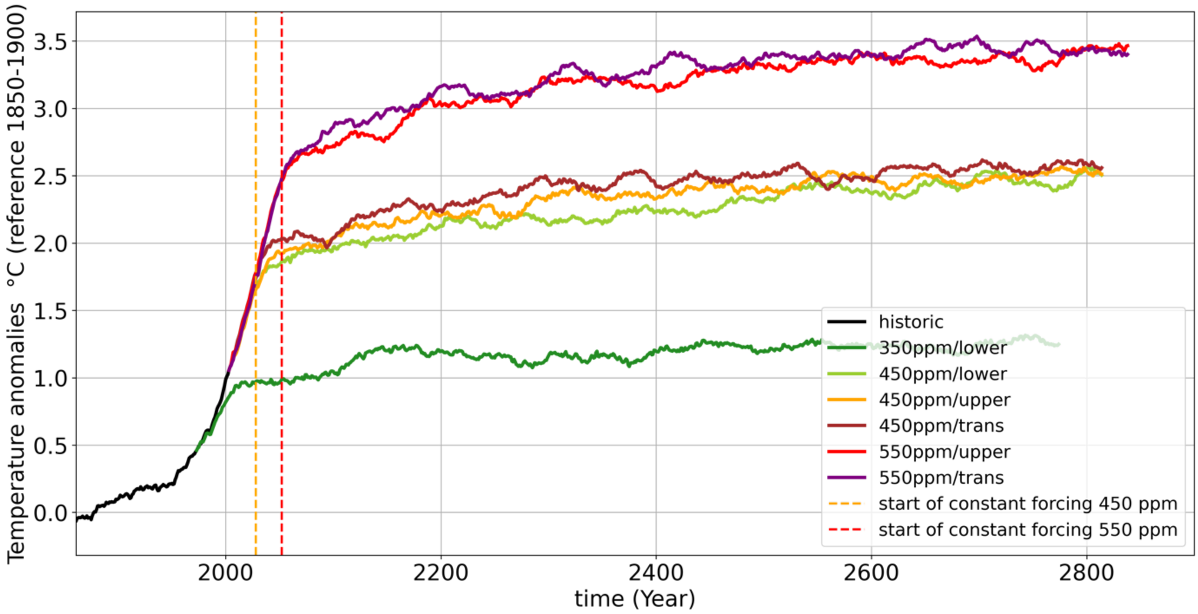

Fig. S9. Global mean land precipitation in a 30-year running mean for the different experiments, including the historic period until 2019 in black. Precipitation increases mainly due to increasing temperatures, which increases evapotranspiration and humidity in the air. This effect is offset by a decrease of evapotranspiration in managed land. Therefore, a loss of natural land, leads to a decrease in evapotranspiration, humidity and consequently precipitation.

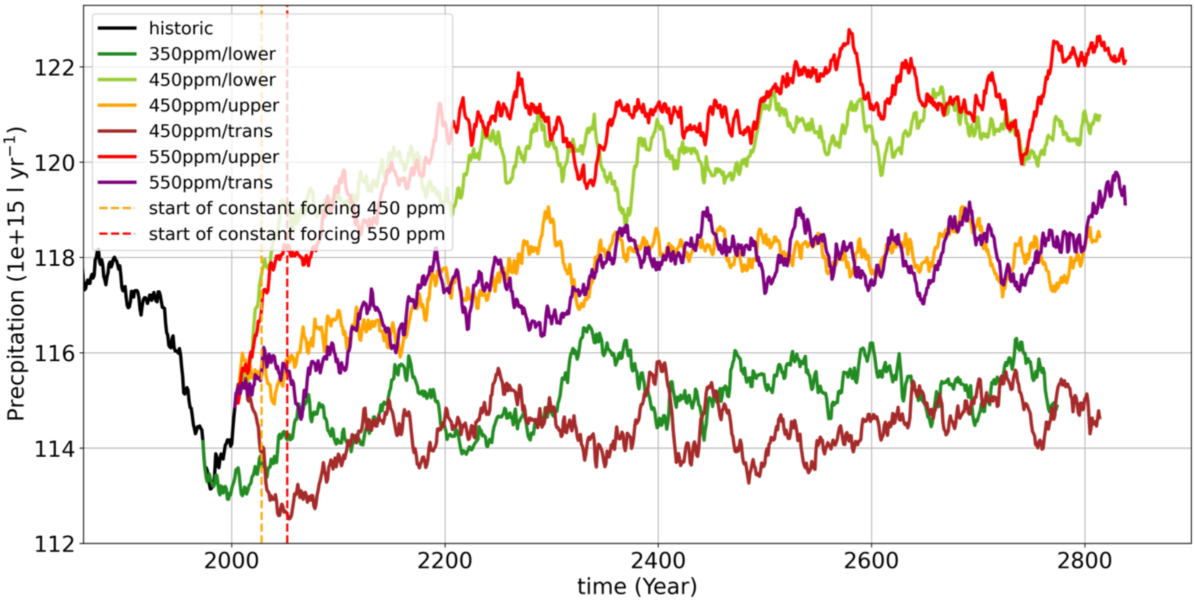

Table S1. Summary of key NPP and HANPP results from the LPJmL4 biosphere model simulations.

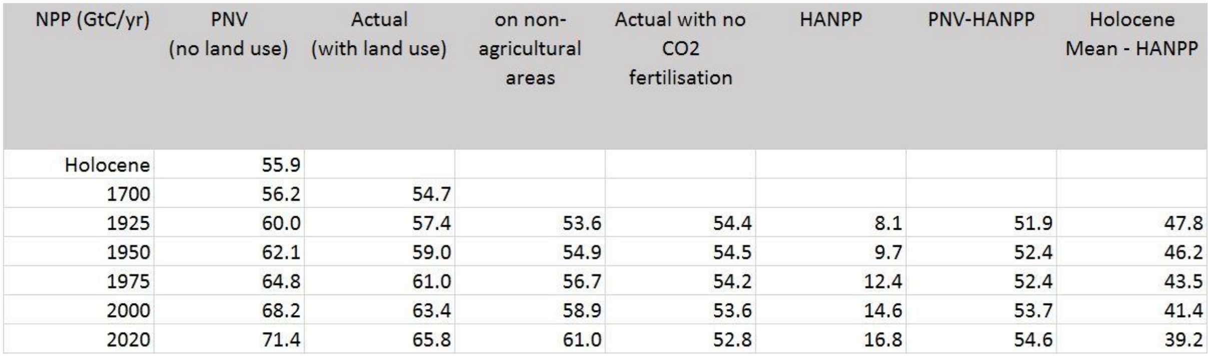

NPP (GtC/yr)	PNV (no land use)	Actual (with land use)	on non-agricultural areas	Actual with no CO2 fertilisation	HANPP	PNV-HANPP	Holocene Mean - HANPP
Holocene	55.9						
1700	56.2	54.7					
1925	60.0	57.4	53.6	54.4	8.1	51.9	47.8
1950	62.1	59.0	54.9	54.5	9.7	52.4	46.2
1975	64.8	61.0	56.7	54.2	12.4	52.4	43.5
2000	68.2	63.4	58.9	53.6	14.6	53.7	41.4
2020	71.4	65.8	61.0	52.8	16.8	54.6	39.2

Table S2: Land carbon exchange with the atmosphere (negative – land sink, positive – land source) and temperature increase over land and globally between the years 1988 and 2100 (green) and 1988 and 2770 (orange). Note: Additional terrestrial carbon stock increase from pre-industrial to 1988 is 34.75 GtC, temperature warming from pre-industrial to 1988 is +0.58°C over land and 0.54°C globally.

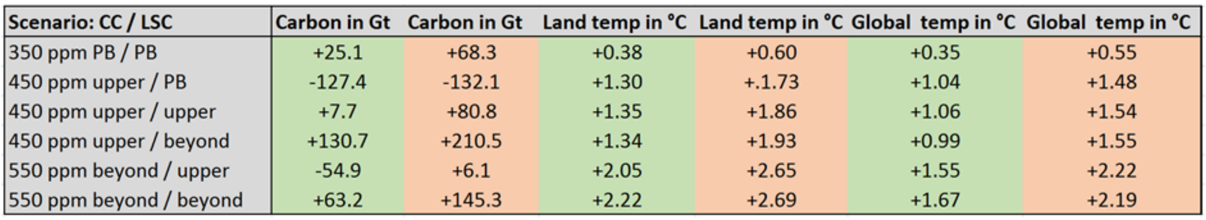

Scenario: CC / LSC	Carbon in Gt	Carbon in Gt	Land temp in °C	Land temp in °C	Global temp in °C	Global temp in °C
350 ppm PB / PB	+25.1	+68.3	+0.38	+0.60	+0.35	+0.55
450 ppm upper / PB	-127.4	-132.1	+1.30	+.1.73	+1.04	+1.48
450 ppm upper / upper	+7.7	+80.8	+1.35	+1.86	+1.06	+1.54
450 ppm upper / beyond	+130.7	+210.5	+1.34	+1.93	+0.99	+1.55
550 ppm beyond / upper	-54.9	+6.1	+2.05	+2.65	+1.55	+2.22
550 ppm beyond / beyond	+63.2	+145.3	+2.22	+2.69	+1.67	+2.19

Table S3. Model simulations and empirically derived results (initially (1988-2018) and at the end of the three experiments): Sea surface temperature (SST), average temperature in the upper 500 m ($T_{0\text{-}500m}$), primary production (PP), new production (NP), particulate organic C-flux at 500 m depth (F_{500m}), total ocean inventory of DIC (DIC_{tot}) and in the upper 1000 m (DIC_{1000m}), and the saturation state of aragonite (Ω). Empirically derived fluxes (NP-E, F_{500m}-E) are shown for new production and particulate organic C-export at 500 m depth.

Exp. ppm	SST *ºC*	$T_{0\text{-}500m}$ *ºC*	PP $GtC\ yr^{-1}$	NP $GtC\ yr^{-1}$	NP-E $GtC\ yr^{-1}$	F_{500m} $GtC\ yr^{-1}$	F_{500m}-E $GtC\ yr^{-1}$	DIC_{tot} *Eg C*	DIC_{1000m} *Eg C*	Ω
ini(1988)	18.8	11.3	50.2	8.5	8.8	1.59	1.70	38.4	9.1	3.2
350	19.1	11.7	51.3	8.6	9.0	1.62	1.73	38.7	9.1	3.2
450	19.8	12.3	51.3	8.5	8.9	1.59	1.64	39.1	9.2	2.8
550	20.5	12.8	51.3	8.3	8.7	1.54	1.54	39.3	9.3	2.5

REFERENCES

1. J. Rockström, W. Steffen, K. Noone, Å. Persson, S. Chapin, E. F. Lambin, T. M. Lenton, M. Scheffer, C. Folke, J. Schellnhuber, B. Nykvist, C. A. DeWit, T. Hughes, S. van der Leeuw, H. Rodhe, S. Sörlin, P. K Snyder, R. Costanza, U. Svedin, M. Falkenmark, L. Karlberg, R. W. Corell, V. J. Fabry, J. Hansen, D. Liverman, K. Richardson, P. Crutzen, J. Foley, A safe operating space for humanity. *Nature* **461**, 472–475 (2009).

2. W. Steffen, K. Richardson, J. Rockström, S. E. Cornell, I. Fetzer, E. M. Bennett, R. Biggs, S. R. Carpenter, W. de Vries, C. A. de Wit, C. Folke, D. Gerten, J. Heinke, G. M. Mace, L. M. Persson, V. Ramanathan, B. Reyers, S. Sörlin, Planetary boundaries: Guiding human development on a changing planet. *Science* **347**, 1259855 (2015).

3. W. Steffen, K. Richardson, J. Rockström, H. Schellnhuber, O. P. Dube, S. Dutreil, T. M. Lenton, J. Lubchenco, The emergence and evolution of Earth system science. *Nat. Rev. Earth Environ.* **1**, 54–63 (2020).

4. J. Zalasiewicz, C. N. Waters, C. Summerhayes, A. P. Wolfe, A. D. Barnosky, A. Cearreta, P. Crutzen, E. C. Ellis, J. J. Fairchild, A. Gałuszka, P. Haff, I. Hajdas, M. J. Head, J. A. I. do Sul, C. Jeandel, R. Leinfelder, J. R. McNeill, C. Neal, E. Odada, N. Oreskes, W. Steffen, J. P. M. Syvitski, M. Wagreich, M. Williams, The working group on the 'Anthropocene': Summary of evidence and recommendations. *Anthropocene* **19**, 55–60 (2017).

5. C. N. Waters, J. Zalasiewicz, C. Summerhayes, A. D. Barnosky, C. Poirier, A. Gałuszka, A. Cearreta, M. Edgeworth, E. C. Ellis, M. Ellis, C. Jeandel, R. Leinfelder, J. R. McNeill, D. D. Richter, W. Steffen, J. Syvitski, D. Vidas, M. Wagreich, M. Williams, A. Zhisheng, J. Grinevald, E. Odada, N. Oreskes, A. P. Wolfe, The Anthropocene is functionally and stratigraphically distinct from the Holocene. *Science* **351**, eaad2622 (2016).

6. W. F. Ruddiman, *Earth's Climate: Past and Future* (Third edition, W.H. Freeman and Co., 2014).

7. C. P. Summerhayes, *Paleoclimatology: From Snowball Earth to the Anthropocene* (Wiley-Blackwell, 2020).

8. H.-J. Schellnhuber, Discourse: Earth system analysis—The scope of the challenge, in *Earth System Analysis: Integrating Science for Sustainability*. H.-J. Schellnhuber, V. Wenzel, Eds. (Springer, Heidelberg, 1998), pp. 3–195.

9. M. B. Osman, J. E. Tierney, J. Zhu, R. Tardif, G. J. Hakim, J. King, C. J. Poulsen, Globally resolved surface temperatures since the Last Glacial Maximum. *Nature* **599**, 239–244 (2021).

10. R. M. Beyer, M. Krapp, A. Manica, High-resolution terrestrial climate, bioclimate and vegetation for the last 120,000 years. *Sci. Data.* **7**, 236 (2020).

11. P. K. Snyder, C. Delire, J. A. Foley, Evaluating the influence of different vegetation biomes on the global climate. *Clim. Dyn.* **23**, 279–302 (2004).

12. P. C. West, G. T. Narisma, C. C. Barford, C. J. Kucharik, J. A. Foley, An alternative approach for quantifying climate regulation by ecosystems. *Front. Ecol. Environ.* **9**, 126–133 (2010).

13. S. J. Lade, W. Steffen, W. de Vries, S. R. Carpenter, J. F. Donges, D. Gerten, H. Hoff, T. Newbold, K. Richardson, J. Rockström, Human impacts on planetary boundaries amplified by Earth system interactions. *Nat. Sustain.* **3**, 119–128 (2020).

14. A. Chrysafi, V. Virkki, M. Jalava, V. Sandström, J. Piipponen, M. Porkka, S. Lade, K. La Mere, L. Wang-Erlandsson, L. Scherer, L. Andersen, E. Bennett, K. Brauman, G. Cooper, A. De Palma, P. Döll, A. Downing, T. DuBois, I. Fetzer, E. Fulton, D. Gerten, H. Jaafar, J. Jaegermeyr, F. Jaramillo, M. Jung, H. Kahiluoto, A. Mackay, L. Lassaletta, D. Mason-D'Croz, M. Mekonnen, K. Nash, A. Pastor, N. Ramankutty, B. Ridoutt, S. Siebert, B. Simmons, A. Staal, Z. Sun, A. Tobian, A. Usubiaga-Liaño, R. van der Ent, A. van Soesbergen, P. Verburg, Y. Wada, S. Zipper, M. Kummu, Quantifying Earth system interactions for sustainable food production: An expert elicitation. *Nat. Sustain.* **5**, 830–842 (2022).

15. Intergovernmental Panel on Climate Change, *Climate Change 2022: Impacts, Adaptation, and Vulnerability,* H.-O. Pörtner, D. C. Roberts, M. Tignor, E. S. Poloczanska, K. Mintenbeck, A. Alegría, M. Craig, S. Langsdorf, S. Löschke, V. Möller, A. Okem, B. Rama, Eds. (Cambridge Univ. Press, 2022).

16. E. S. Brondizio, J. Settele, S. Díaz, H. T. Ngo, *Global Assessment Report on Biodiversity and Ecosystem Services of the Intergovernmental Science-Policy Platform on Biodiversity and Ecosystem Services* (IPBES, 2019).

17. Intergovernmental Panel on Climate Change, *Climate Change 2021: The Physical Science Basis* (Cambridge University Press, 2021).

18. D. A. McKay, A. Staal, J. Abrams, R. Winkelmann, B. Sakschewski, S. Loriani, I. Fetzer, S. E. Cornell, J. Rockström, T. M. Lenton, Exceeding 1.5°C global warming could trigger multiple climate tipping points. *Science* **377**, eabn7950 (2022).

19. Past Interglacials Working Group of PAGES, Interglacials of the last 800,000 years. *Rev. Geophys.* **54**, 162–219 (2016).

20. C. Ragon, V. Lembo, V. Lucarini, C. Vérard, J. Kasparian, M. Brunetti, Robustness of competing climatic states. *J. Clim.* **35**, 2769–2784 (2022).

21. J. M. Anderies, S. R. Carpenter, W. Steffen, J. Rockström, The topology of non-linear global carbon dynamics: From tipping points to planetary boundaries. *Environ. Res. Lett.* **8**, 044048 (2013).

22. S. J. Lade, J. Norberg, J. Anderies, C. Beer, S. Cornell, J. Donges, I. Fetzer, T. Gasser, K. Richardson, J. Rockström, W. Steffen, Potential feedbacks between loss of biosphere integrity and climate change. *Glob. Sust.* **2**, 1–15 (2019).

23. M. Exposito-Alonso, T. R. Booker, L. Czech, T. Fukami, L. Gillespie, S. Hateley, C. C. Kyriazis, P. L. M. Lang, L. Leventhal, D. Nogues-Bravo, V. Pagowski, M. Ruffley, J. P. Spence, S. E. Toro Arana, C. L. Weiß, E. Zess, Genetic diversity loss in the Anthropocene. *Science* **377**, 1431–1435 (2022).

24. H. Ceballos, P. R. Ehrlich, A. D. Barnosky, A. García, R. M. Pringle, T. M. Palmer, Accelerated modern human–induced species losses: Entering the sixth mass extinction. *Sci. Adv.* **1**, e1400253 (2015).

25. M. D. A. Rounsevell, M. Harfoot, P. A. Harrison, T. Newbold, R. D. Gregory, G. M. Mace, A biodiversity target based on species extinctions. *Science* **368**, 1193–1195 (2020).

26. R. H. Cowie, P. Bouchet, B. Fontaine, The sixth mass extinction: Fact, fiction or speculation? *Biol. Rev.* **97**, 640–663 (2022).

27. R. J. Scholes, R. Biggs, A Biodiversity Intactness Index. *Nature* **434**, 45–49 (2005).

28. P. A. Martin, R. E. Green, A. Balmford, The Biodiversity Intactness Index may underestimate losses. *Nat. Evol.* **3**, 862–863 (2019).

29. S. E. Jorgensen, Y. M. Svirezhev, *Towards a Thermodynamic Theory for Ecological Systems* (Elsevier, 2004).

30. A. Kleidon, Sustaining the terrestrial biosphere in the anthropocene: A thermodynamic Earth system perspective. *Ecol. Economy Soc. INSEE J.* **6**, 53–80 (2023).

31. S. W. Running, A measurable planetary boundary for the biosphere. *Science* **337**, 1458–1459 (2012).

32. H. Haberl, K. H. Erb, F. Krausmann, Human appropriation of net primary production: Patterns, trends, and planetary boundaries. *Annu. Rev. Environ. Res.* **39**, 363–391 (2014).

33. F. Krausmann, K. H. Erb, S. Gingrich, H. Haberl, A. Bondeau, V. Gaube, C. Lauka, C. Plutzar, T. D. Searchinger, Global human appropriation of net primary production doubled in the 20th century. *Proc. Natl. Acad. Sci. U.S.A.* **110**, 10324–10329 (2013).

34. L. V. Gatti, L. S. Basso, J. B. Miller, M. Gloor, L. G. Dominigues, H. L. G. Cassol, G. Tejada, L. E. O. C. Aragao, C. Nobre, W. Peters, L. Marani, E. Arai, A. H. Sanches, S. M. Correa, L. Anderson, C. Von Randow, C. S. C. Correia, S. P. Crispim, R. A. L. Neves, Amazonia as a carbon source linked to deforestation and climate change. *Nature* **595**, 388–393 (2021).

35. K. Goldewijk, A. Beusen, J. Doelman, E. Stehfest, Anthropogenic land use estimates for the Holocene – HYDE 3.2. *Earth Syst. Sci. Data* **9**, 927–953 (2017).

36. D. Gerten, V. Heck, J. Jägermeyr, B. L. Bodirsky, I. Fetzer, M. Jalava, M. Kummu, W. Lucht, J. Rockström, S. Schaphoff, H. J. Schellnhuber. Feeding ten billion people is possible within four terrestrial planetary boundaries. *Nat. Sust.* **3**, 200–208 (2020).

37. S. Ostberg, W. Lucht, S. Schaphoff, D. Gerten, Critical impacts of global warming on land ecosystems. *Earth Syst. Dyn.* **4**, 347–357 (2013).

38. W. Schwartz, E. Sala, S. Tracey, R. Watson, D. Pauly, The spatial expansion and ecological footprint of fisheries (1950 to present). *PLOS ONE* **5**, e15143 (2010).

39. J. S. Link, R. A. Watson, Global ecosystem overfishing: Clear delineation within real limits to production. *Sci. Adv.* **5**, eaav047 (2019).

40. B. Planque, J.-M. Fromentin, P. Cury, K. F. Drinkwater, S. Jennings, R. I. Perry, S. Kifani, How does fishing alter marine populations and ecosystems sensitivity to climate? *J. Mar. Sys.* **79**, 403–417 (2010).

41. P. M. Forster, C. J. Smith, T. Walsh, W. F. Lamb, M. D. Palmer, K. von Schuckmann, B. Trewin, M. Allen, R. Andrew, A. Birt, A. Borger, T. Boyer, J. A. Broersma, L. Cheng, F. Dentener, P. Friedlingstein, N. Gillett, J. M. Gutiérrez, J. Gütschow, M. Hauser, B. Hall, M. Ishii, S. Jenkins, R. Lamboll, X. Lan, J.-Y. Lee, C. Morice, C. Kadow, J. Kennedy, R. Killick, J. Minx, V. Naik, G. Peters, A. Pirani, J. Pongratz, A. Ribes, J. Rogelj, D. Rosen, C.-F. Schleussner, S. Seneviratne, S. Szopa, P. Thorne, R. Rohde, M. Rojas Corradi, D. Schumacher, R. Vose, K. Zickfeld, X. Zhang, V. Masson-Delmotte, P. Zhai, Indicators of Global Climate Change 2022: Annual update of large-scale indicators of the state of the climate system and the human influence. *Earth Syst. Sci. Data* **15**, 2295–2327 (2023).

42. H. Schellnhuber, S. Rahmstorf, R. Winkelmann, Why the right climate target was agreed in Paris. *Nat. Clim. Change* **6**, 649–653 (2016).

43. L. Persson, B. Almroth, C. Collins, S. Cornell, C. de Wit, M. Diamond, P. Fantke, M. Hassellöv, M. MacLeod, M. Ryberg, P. Jørgensen, P. Villarrubia-Gómez, Z. Wang, M. Zwicky Hauschild, Outside the safe operating space of the planetary boundary for novel entities. *Environ. Sci. Tech.* **56**, 1510–1521 (2022).

44. P. J. Nair, L. Froidevaux, J. Kuttippurath, J. M. Zawodny, J. M. Russell III, W. Steinbrecht, H. Claude, T. Leblanc, J. A. E. van Gijsel, B. Johnson, D. P. J. Swart, A. Thomas, R. Querel, R. Wang, J. Anderson, Subtropical and midlatitude ozone trends in the stratosphere: Implications for recovery. *J. Geophys. Res. Atmos.* **120**, 7247–7257 (2015).

45. A. Pazmiño, S. Godin-Beekmann, A. Hauchecorne, C. Claud, S. Khaykin, F. Goutail, E. Wolfram, J. Salvador, E. Quel, Multiple symptoms of total ozone recovery inside the Antarctic vortex during austral spring. *Atmospheric Chem. Phys.* **18**, 7557–7572 (2018).

46. M. Porkka, V. Virkki, L. Wang-Erlandsson, D. Gerten, T. Gleeson, C. Mohan, I. Fetzer, F. Jaramillo, A. Staal, S. te Wierik, A. Tobian, R. van der Ent, P. Döll, M. Flörke, S. N. Gosling, N. Hanasaki, Y. Satoh, H. M. Schmied, N. Wanders, J. Rockström, M. Kummu, Global water cycle shifts far beyond pre-industrial conditions – Planetary boundary for freshwater change transgressed (2023); https://eartharxiv.org/repository/view/3438/.

47. T. Gleeson, L. Wang-Erlandsson, S. C. Zipper, M. Porkka, F. Jaramillo, D. Gerten, I. Fetzer, S. E. Cornell, L. Piemontese, L. J. Gordon, J. Rockström, T. Oki, M. Sivapalan, Y. Wada, K. A. Brauman, M. Flörke, M. F. P. Bierkens, B. Lehner, P. Keys, M. Kummu, T. Wagener, S. Dadson, T. J. Troy, W. Steffen, M. Falkenmark, J. S. Famiglietti, The water planetary boundary: Interrogation and revision. *One Earth.* **2**, 223–234 (2020).

48. L. Wang-Erlandsson, A. Tobian, R. J. van der Ent, I. Fetzer, S. te Wierik, M. Porkka, A. Staal, F. Jaramillo, H. Dahlmann, C. Singh, P. Greve, D. Gerten, P. W. Keys, T. Gleeson, S. E. Cornell, W. Steffen, X. Bai, J. Rockström, A planetary boundary for green water. *Nat. Rev. Earth Environ.* **3**, 380–392 (2022).

49. Y. Qin, N. D. Mueller, S. Siebert, R. B. Jackson, A. A. Kouchak, J. B. Zimmerman, D. Tong, C. Hong, S. J. Davis, Flexibility and intensity of global water use. *Nat. Sustain.* **2**, 515–523 (2019).

50. K. S. Carslaw, H. Gordon, D. S. Hamilton, J. S. Johnson, L. A. Regayre, M. Yoshioka, K. J. Pringle, Aerosols in the pre-industrial atmosphere. *Curr. Clim. Chang. Rep.* **3**, 1–15 (2017).

51. N. Bellouin, J. Quaas, E. Gryspeerdt, S. Kinne, P. Stier, D. Watson-Parris, O. Boucher, K. S. Carslaw, M. Christensen, A.-L. Daniau, J.-L. Dufresne, G. Feingold, S. Fiedler, P. Forster, A. Gettelman, J. M. Haywood, U. Lohmann, F. Malavelle, T. Mauritsen, D. T. McCoy, G. Myhre, J. Mülmenstädt, D. Neubauer, A. Possner, M. Rugenstein, Y. Sato, M. Schulz, S. E. Schwartz, O. Sourdeval, T. Storelvmo, V. Toll, D. Winker, B. Stevens, Bounding global aerosol radiative forcing of climate change. *Rev. Geophys.* **58**, e2019RG000660 (2020).

52. J. Hooper, S. K. Marx, A global doubling of dust emissions during the Anthropocene? *Glob. Planet. Change* **169**, 70–91 (2018).

53. P. Kinppertz, M. C. Todd, Mineral dust aerosols over the Sahara: Meteorological controls on emission and transport and implications for modeling. *Rev. Geophys.* **50**, RG1007 (2012).

54. M. L. Griffiths, K. R. Johnson, F. S. R. Pausata, J. C. White, G. M. Henderson, C. T. Wood, H. Yang, V. Ersek, C. Conrad, N. Sekhon, End of Green Sahara amplified mid- to late Holocene megadroughts in mainland Southeast Asia. *Nat. Commun.* **11**, 4204 (2020).

55. M. Chin, T. Diehl, Q. Tan, J. M. Prospero, R. A. Kahn, L. A. Remer, H. Yu, A. M. Sayer, H. Bian, I. V. Geogdzhayev, B. N. Holben, S. G. Howell, B. J. Huebert, N. C. Hsu, D. Kim, T. L. Kucsera, R. C. Levy, M. I. Mishchenko, X. Pan, P. K. Quinn, G. L. Schuster, D. G. Streets, S. A. Strode, O. Torres, X.-P. Zhao, Multi-decadal aerosol variations from 1980 to 2009: A perspective from observations and a global model. *Atmos. Chem. Phys.* **14**, 3657–3690 (2014).

56. L. Sogacheva, T. Popp, A. M. Sayer, O. Dubovik, M. J. Garay, A. Heckel, N. C. Hsu, H. Jethva, R. A. Kahn, P. Kolmonen, M. Kosmale, G. de Leeuw, R. C. Levy, P. Litvinov, A. Lyapustin, P. North, O. Torres, Merging regional and global AOD records from 15 available satellite products. *Atmos. Chem. Phys.* **20**, 2031–2056 (2019).

57. A. Vogel, G. Alessa, R. Scheele, L. Weber, O. Dubovik, P. North, S. Fiedler, Uncertainty in aerosol optical depth from modern aerosol-climate models, reanalyses, and satellite products. *J. Geophys. Res. Atmos.* **127**, e2021JD035483 (2022).

58. J. Haywood, A. Jones, N. Bellouin, D. Stephenson, Asymmetric forcing from stratospheric aerosols impacts Sahelian rainfall. *Nat. Clim. Change.* **3**, 660–665 (2013).

59. K. S. Krishnamohan, G. Bala, Sensitivity of tropical monsoon precipitation to the latitude of stratospheric aerosol injections. *Clim. Dyn.* **59**, 151–168 (2022).

60. S. Roose, G. Bala, K. S. Krishnamohan, L. Cao, K. Caldeira, Quantification of tropical monsoon precipitation changes in terms of interhemispheric differences in stratospheric sulfate aerosol optical depth. *Clim. Dyn.* **2023**, 1–16 (2023).

61. A. Donohoe, J. Marshall, D. Ferreira, D. Mcgee, The relationship between ITCZ location and cross-equatorial atmospheric heat transport: From the seasonal cycle to the last glacial maximum. *J. Clim.* **26**, 3597–3618 (2013).

62. M. C. MacCracken, H.-J. Shin, K. Caldeira, G. A. Ban-Weiss, Climate response to imposed solar radiation reductions in high latitudes. *Earth Syst. Dyn.* **4**, 301–315 (2013).

63. N. Devaraju, G. Bala, A. Modak, Effects of large-scale deforestation on precipitation in the monsoon regions: Remote versus local effects. *Proc. Natl. Acad. Sci. U.S.A.* **112**, 3257–3262 (2015).

64. I. B. Ocko, V. Ramaswamy, Y. Ming, Contrasting climate responses to the scattering and absorbing features of anthropogenic aerosol forcings. *J. Clim.* **27**, 5329–5345 (2014).

65. M. Zhao, L. Cao, G. Bala, L. Duan, Climate response to latitudinal and altitudinal distribution of stratospheric sulfate aerosols. *J. Geophys. Res. Atmos.* **126**, e2021JD035379 (2021).

66. J. T. Fasullo, B. L. Otto-Bliesner, S. Stevenson, The influence of volcanic aerosol meridional structure on monsoon responses over the last millennium. *Geophys. Res. Lett.* **46**, 12350–12359 (2019).

67. S. Fiedler, T. Crueger, R. D’Agostino, K. Peters, T. Becker, D. Leutwyler, L. Paccini, J. Burdanowitz, S. Buehler, A. Uribe, T. Dauhut, D. Dommenget, K. Fraedrich, L. Jungandreas, N. Maher, A. Naumann, M. Rugenstein, M. Sakradzija, H. Schmidt, F. Sielmann, C. Stephan, C. Timmreck, X. Zhu, B. Stevens, Simulated tropical precipitation assessed across three major phases of the Coupled Model Intercomparison Project (CMIP). *Mon. Weather Rev.* **148**, 3653–3680 (2020).

68. P. Zanis, D. Akritidis, A. K. Georgoulias, R. J. Allen, S. E. Bauer, O. Boucher, J. Cole, B. Johnson, M. Deushi, M. Michou, J. Mulcahy, P. Nabat, D. Olivié, N. Oshima, A. Sima, M. Schulz, T. Takemura, K. Tsigaridis, Fast responses on pre-industrial climate from present-day aerosols in a CMIP6 multi-model study. *Atmos. Chem. Phys.* **20**, 8381–8404 (2020).

69. S. Fiedler, B. Stevens, M. Gidden, S. J. Smith, K. Riahi, D. van Vuuren, First forcing estimates from the future CMIP6 scenarios of anthropogenic aerosol optical properties and an associated Twomey effect. *Geosci. Model Dev.* **12**, 989–1007 (2019).

70. N. M. Mahowald, R. Scanza, J. Brahney, C. L. Goodale, P. G. Hess, J. K. Moore, J. Neff, Aerosol deposition impacts on land and ocean carbon cycles. *Curr. Clim. Change Rep.* **3**, 16–31 (2017).

71. L. Jiang, R. A. Feely, B. R. Carter, D. J. Greeley, D. K. Gledhill, K. M. Arzayus, Climatological distribution of aragonite saturation state in the global oceans. *Glob. Biogeochem. Cycles.* **29**, 1656–1673 (2015).

72. EU Copernicus Climate Change Service, “Land cover classification gridded maps from 1992 to present derived from satellite observations”, ICDR Land Cover 2016–2020.

73. Food and Agricultural Organization of the United Nations, (FAO), United Nations’ Environmental Program, (UNEP), “The State of the World’s Forests 2020. Forests, biodiversity and people” (Publication 978-92-5-132419-6, 2020); https://doi.org/10.4060/ca8642en.

74. Food and Agricultural Organization of the United Nations, (FOA), “Global Forest Resources Assessment 2020: Main report” (Publication 978-92-5-132974-0, 2020); https://doi.org/10.4060/ca9825en.

75. S. R. Carpenter, E. M. Bennett, Reconsideration of the planetary boundary for phosphorus. *Environ. Res. Lett.* **6**, 014009 (2011).

76. C. Liu, H. Tian, Global nitrogen and phosphorus fertilizer use for agriculture production in the past half century: Shifted hot spots and nutrient imbalance. *Earth Syst. Sci. Data* **9**, 181–192 (2017).

77. W. J. Brownlie, M. A. Sutton, K. V. Heal, D. S. Reay, B. M. Spears (eds.), *Our Phosphorus Future* (U.K. Centre for Ecology & Hydrology, 2022).

78. T. Zou, X. Zhang, E. Davidson, Improving phosphorus use efficiency in cropland to address phosphorus challenges by 2050. *Earth Space Sci. Open Archive* (2020). https://doi.org/10.1002/essoar.10504095.1

79. D. Cordell, S. White, Life's bottleneck: Sustaining the World's phosphorus for a food secure future. *Annu. Rev. Environ. Res.* **39**, 161–188 (2014).

80. Food and Agriculture Organisation of the United Nations (FAO), "World fertilizer trends and outlook to 2022 – Summary Report, Rome" (2019); www.fao.org/3/ca6746en/ca6746en.pdf)

81. M. A. Adams, N. Buchmann, J. Sprent, T. N. Buckley, T. L. Turnbull, Crops, nitrogen, water: Are legumes friend, foe, or misunderstood ally? *Trends Plant. Sci.* **23**, 539–550 (2018).

82. P. M. Vitousek, D. N. L. Menge, S. C. Reed, C. C. Cleveland, Biological nitrogen fixation: Rates, patterns and ecological controls in terrestrial ecosystems. *Philos. Trans. R. Soc. Lond. B. Biol. Sci.* **368**, 1621 (2013).

83. M. V. B. Figueiredo, A. E. S. Mergulhão, J. K. Sobral, M. A. L. Junio, A. S. F. Araújo, Biological nitrogen fixation: Importance, associated diversity, and estimates, in *Plant Microbe Symbiosis: Fundamentals and Advances* (Springer, 2013), pp. 267–289.

84. FAO, "FAOSTAT—FAO database for food and agriculture" (2022); www.fao.org/faostat/ (accessed 4.19.22)

85. M. Drüke, W. von Bloh, S. Petri, B. Sakschewski, S. Schaphoff, M. Forkel, W. Huiskamp, G. Feulner, K. Thonicke, CM2Mc-LPJmL v1.0: Biophysical coupling of a process-based dynamic vegetation model with managed land to a general circulation model. *Geosci. Model. Dev.* **14**, 4117–4141 (2021).

86. K.-H. Erb, T. Kastner, C. Plutzar, A. L. S. Bais, N. Carvalhais, T. Fetzel, S. Gingrich, H. Haberl, C. Lauk, M. Niedertscheider, J. Pongratz, M. Thurner, S. Luyssaert, Unexpectedly large impact of forest management and grazing on global vegetation biomass. *Nature* **553**, 73–76 (2017).

87. Y. M. Bar-On, R. Phillips, R. Milo, The biomass distribution on Earth. *Proc. Natl. Acad. Sci. U.S.A.* **115**, 6506–6511 (2018).

88. K. Matsuomoto, T. Hashioka, Y. Yamanaka, Effect of temperature-dependent organic carbon decay on atmospheric pCO_2. *J. Geophys. Res.* **112**, G02007 (2007).

89. L. Kwiatkowski, O. Torres, L. Bopp, O. Aumont, M. Chamberlain, J. R. Christian, J. P. Dunne, M. Gehlen, T. Ilyina, J. G. John, A. Lenton, H. Li, N. S. Lovenduski, J. C. Orr, J. Palmieri, Y. Santana-Falcón, J. Schwinger, R. Séférian, C. A. Stock, A. Tagliabue, Y. Takano, J. Tjiputra, K. Toyama, H. Tsujino, M. Watanabe, A. Yamamoto, A. Yool, T. Ziehn, Twenty-first century ocean warming,

acidification, deoxygenation, and upper-ocean nutrient and primary production decline from CMIP6 model projections. *Biogeosci* **17**, 3439–3470 (2020).

90. E. A. Laws, E. D'Sa, P. Naik, Simple equations to estimate ratios of new or export production to total production from satellite-derived estimates of sea surface temperature and primary production. *Limnol. Oceanogr. Meth.* **9**, 593–601 (2011).

91. C. M. Marsay, R. J. Sanders, S. A. Henson, K. Pabortsava, E. P. Achterberg, R. S. Lampitt, Attenuation of sinking POC flux in the mesopelagic. *Proc. Natl. Acad. Sci. U.S.A.* **112**, 1089–1094 (2015).

92. K. A. Chrichton, J. D. Wilson, A. Ridgewell, F. Boscob-Galazzo, E. H. John, B. S. Wade, P. N. Pearson, What the geological past can tell us about the future of the ocean's twilight zone. *Nat. Commun.* **14**, 2376 (2023).

93. The Royal Society, "Ocean acidification due to increasing atmospheric carbon dioxide" (Publication 0 85403 617 2, Policy Doc. 12/05, R. Soc., 2005).

94. E. D. Galbraith, J. P. Dunne, A. Gnanadesikan, R. D. Slater, J. L. Sarmiento, C. O. Dufour, G. F. de Souza, D. Bianchi, M. Claret, K. B. Rodgers, S. S. Marvasti, Complex functionality with minimal computation: Promise and pitfalls of reduced-tracer ocean biogeochemistry models. *J. Adv. Model Earth Syst.* **7**, 2012–2028 (2015).

95. S. Schaphoff, M. Forkel, C. Müller, J. Knauer, W. von Bloh, D. Gerten, J. Jägermeyr, W. Lucht, A. Rammig, K. Thonicke, K. Waha, LPJmL4 – A dynamic global vegetation model with managed land – Part 2: Model evaluation. *Geosci. Model Dev.* **11**, 1377–1403 (2018b).

96. NASA Earth Observation, "AURA Ozone data"; https://neo.gsfc.nasa.gov/archive/geotiff.float/AURA_OZONE_M/.

97. N. Ramankutty, J. A. Foley, Characterizing patterns of global land use: An analysis of global croplands data. *Glob. Biogeochem. Cycles.* **12**, 667–685 (1998).

98. C. W. Snyder, M. D. Mastrandrea, S. H. Schneider, The complex dynamics of the climate system: Constraints on our knowledge, policy implications and the necessity of systems thinking. *Philos. Complex Syst.* **10**, 467–505 (2011).

99. M. Willeit, A. Ganopolski, R. Calov, V. Brovkin, Mid-Pleistocene transition in glacial cycles explained by declining CO_2 and regolith removal. *Sci. Adv.* **5**, eaav7337 (2019).

100. J. Zheng, J. L. Payne, A. Wagner, Cryptic genetic variation accelerates evolution by opening access to diverse adaptive peaks. *Science* **365**, 347–353 (2019).

101. M. C. Bitter, L. Kapsenberg, J.-P. Gattuso, C. A. Pfister. Standing genetic variation fuels rapid adaptation to ocean acidification. *Nat. Commun.* **10**, 5821 (2019).

102. T. H. Oliver, M. S. Heard, N. J. Isaac, D. B Roy, D. Procter, F. Eigenbrod, R. Freckleton, A. Hector, C. D. L. Orme, O. L. Petchey, V. Proença, Biodiversity and resilience of ecosystem functions. *Trends Ecol. Evol.* **30**, 673–684 (2015).

103. A. A. Hoffmann, C. M. Sgrò, T. N. Kristensen, Revisiting adaptive potential, population size, and conservation. *Trends Ecol. Evol.* **32**, 506–517 (2017).

104. A. Miraldo, S. Li, M. K. Borregaard, A. Flórez-Rodríguez, S. Gopalakrishnan, M. Rizvanovic, Z. Wang, C. Rahbek, K. A. Marske, D. Nogués-Bravo, An anthropocene map of genetic diversity. *Science* **353**, 1532–1535 (2016).

105. S. Blanchet, J. G. Prunier, H. De Kort, Time to go bigger: Emerging patterns in macrogenetics. *Trends Genet.* **33**, 579–580 (2017).

106. S. Theodoridis, D. A. Fordham, S. C. Brown, S. Li, C. Rahbek, D. Nogues-Bravo, Evolutionary history and past climate change shape the distribution of genetic diversity in terrestrial mammals. *Nat. Commun.* **11**, 2557 (2020).

107. D. M. Leigh, C. B. van Rees, K. L. Millette, M. F. Breed, C. Schmidt, L. D. Bertola, B. K. Hand, M. E. Hunter, E. L. Jensen, F. Kershaw, L. Liggins, G. Luikart, S. Manel, J. Mergeay, J. M. Miller, G. Segelbacher, S. Hoban, I. Paz-Vinas, Opportunities and challenges of macrogenetic studies. *Nat. Rev. Genet.* **22**, 791–807 (2021).

108. S. Theodoridis, C. Rahbek, D. Nogués-Bravo, Exposure of mammal genetic diversity to mid-21st century global change. *Ecography* **44**, 817–831 (2021).

109. S. Hoban, M. Brufordb, J. D'Urban Jackson, M. Lopes-Fernandes, M. Heuertz, P. A. Hohenlohe, I. Paz-Vinas, P. Sjögren-Gulve, G. Segelbacher, C. Vernesi, S. Aitken, L. D. Bertola, P. Bloomer, M. Breed, H. Rodríguez-Correa, W. C. Funk, C. E. Grueber, M. E. Hunter, L. Laikre, Genetic diversity targets and indicators in the CBD post-2020 global biodiversity framework must be improved. *Biol. Conserv.* **248**, 108654 (2020).

110. A. Ganopolski, V. Brovkin, Simulation of climate, ice sheets and CO_2 evolution during the last four glacial cycles with an Earth system model of intermediate complexity. *Clim.* **13**, 1695–1716 (2017).

111. S. Schaphoff, W. Bloh, A. Rammig, K. Thonicke, H. Biemans, M. Forkel, D. Gerten, J. Heinke, J. Jägermeyr, J. Knauer, F. Langerwisch, W. Lucht, C. Müller, S. Rolinski, K. Waha, LPJmL4–a dynamic global vegetation model with managed land – Part 1: Model description. *Geosci. Model Dev.* **11**, 1343–1375 (2018).

112. I. C. Harris, P. D. Jones, "CRU TS3.23: Climatic Research Unit (CRU) Time-Series (TS) Version 3.23 of High Resolution Gridded Data of Month-by-month Variation in Climate (Jan. 1901- Dec. 2014)" (CEDA Archive, 2015); https://catalogue.ceda.ac.uk/uuid/5dca9487dc614711a3a933e44a933ad3

113. I. Harris, P. Jones, T. Osborn, D. Lister, Updated high-resolution grids of monthly climatic observations – The CRU TS3.10 dataset. *Int. J. Climatol.* **34**, 623–642 (2014).

114. D. Kaufman, N. McKay, C. Routson, M. Erb, C. Dätwyler, P. S. Sommer, O. Heiri, B. Davis, Holocene global mean surface temperature, a multi-method reconstruction approach. *Sci. Data* **7**, 201 (2020).

115. H. Haberl, K. H. Erb, F. Krausmann, V. Gaube, A. Bondeau, C. Plutzar, S. Gingrich, W. Lucht, M. Fischer-Kowalski, Quantifying and mapping the human appropriation of net primary production in Earth's terrestrial ecosystems. *Proc. Natl. Acad. Sci. U.S.A.* **104**, 12942–12947 (2007).

116. D. Lawrence, K. Vandecar, Effects of tropical deforestation on climate and agriculture. *Nat. Clim. Change* **5**, 27–36 (2015).

117. P. W. Keys, L. Wang-Erlandsson, L. J. Gordon, Revealing invisible water: Moisture recycling as an ecosystem service. *PLOS ONE* **11**, e0151993 (2016).

118. L. Wang-Erlandsson, I. Fetzer, P. W. Keys, R. J. van der Ent, H. H. G. Savenije, L. J. Gordon, Remote land use impacts on river flows through atmospheric teleconnections. *Hydrol. Earth Syst. Sci.* **22**, 4311–4328 (2018).

119. D. Gerten, H. Hoff, J. Rockström, J. Jägermeyr, M. Kummu, A. V. Pastor, Towards a revised planetary boundary for consumptive freshwater use: Role of environmental flow requirements. *Curr. Opin. Environ. Sustain.* **5**, 551–558 (2013).

120. J. Liu, C. Zang, S. Tian, J. Liu, H. Yang, S. Jia, L. You, B. Liu, M. Zhang, Water conservancy projects in China: Achievements, challenges and way forward. *Glob. Environ. Change* **23**, 633–643 (2013).

121. J. Sillmann, C. W. Stjern, G. Myhre, B. H. Samset, Ø. Hodnebrog, T. Andrews, O. Boucher, G. Faluvegi, P. Forster, M. R. Kasoar, V. V. Kharin, A. Kirkevåg, J.-F. Lamarque, D. J. L. Olivié, T. B. Richardson, D. Shindell, T. Takemura, A. Voulgarakis, F. W. Zwiers, Extreme wet and dry conditions affected differently by greenhouse gases and aerosols. *Nat. Clim. Atmospheric Sci.* **2**, 1–7 (2019).

122. N. L. Poff, J. D. Olden, D. M. Merritt, D. M. Pepin, Homogenization of regional river dynamics by dams and global biodiversity implications. *Proc. Natl. Acad. Sci. U.S.A.* **104**, 5732–5737 (2007).

123. A. Staal, O. A. Tuinenburg, J. H. C. Bosmans, M. Holmgren, E. H. van Nes, M. Scheffer, D. C. Zemp, S. C. Dekker, Forest-rainfall cascades buffer against drought across the Amazon. *Nat. Clim. Change* **8**, 539–543 (2018).

124. A. Günther, A. Barthelmes, V. Huth, H. Joosten, G. Jurasinski, F. Koebsch, J. Couwenberg, Prompt rewetting of drained peatlands reduces climate warming despite methane emissions. *Nat. Commun.* **11**, 1644 (2020).

125. T. Maavara, Q. Chen, K. Van Meter, L. E. Brown, J. Zhang, J. Ni, C. Zarfl, River dam impacts on biogeochemical cycling. *Nat. Rev. Earth Environ.* **1**, 103–116 (2020).

126. N. Boers, N. Marwan, H. M. J. Barbosa, J. Kurths, A deforestation-induced tipping point for the south American monsoon system. *Sci. Rep.* **7**, 41489 (2017).

127. K. Frieler, S. Lange, F. Piontek, C. P. O. Reyer, J. Schewe, L. Warszawski, F. Zhao, L. Chini, S. Denvil, K. Emanuel, T. Geiger, K. Halladay, G. Hurtt, M. Mengel, D. Murakami, S. Ostberg, A. Popp, R. Riva, M. Stevanovic, T. Suzuki, J. Volkholz, E. Burke, P. Ciais, K. Ebi, T. D. Eddy, J. Elliott, E. Galbraith, S. N. Gosling, F. Hattermann, T. Hickler, J. Hinkel, C. Hof, V. Huber, J. Jägermeyr, V. Krysanova, R. Marcé, H. Müller Schmied, I. Mouratiadou, D. Pierson, D. P. Tittensor,

R. Vautard, M. van Vliet, M. F. Biber, R. A. Betts, B. L. Bodirsky, D. Deryng, S. Frolking, C. D. Jones, H. K. Lotze, H. Lotze-Campen, R. Sahajpal, K. Thonicke, H. Tian, Y. Yamagata, Assessing the impacts of 1.5 °C global warming – Simulation protocol of the Inter-Sectoral Impact Model Intercomparison Project (ISIMIP2b). *Geosci. Model Dev.* **10**, 4321–4345 (2017).

128. S. Siebert, M. Kummu, M. Porkka, P. Döll, N. Ramankutty, B. R. Scanlon, A global data set of the extent of irrigated land from 1900 to 2005. *Hydrol. Earth Syst. Sci.* **19**, 1521–1545 (2015).

129. Y. Wada, M. F. P. Bierkens, Sustainability of global water use: Past reconstruction and future projections. *Environ. Res. Lett.* **9**, 104003 (2014).

130. C. Zarfl, A. E. Lumsdon, J. Berlekamp, L. Tydecks, K. Tockner, A global boom in hydropower dam construction. *Aquat. Sci.* **77**, 161–170 (2015).

131. R. J. Keenan, G. A. Reams, F. Achard, J. V. de Freitas, A. Grainger, E. Lindquist, Dynamics of global forest area: Results from the FAO Global Forest Resources Assessment 2015. *For. Ecol. Manag.* **352**, 9–20 (2015).

132. A. Barnosky, E. Hadly, J. Bascompte, E. L. Berlow, J. H. Brown, M. Fortelius, W. M. Getz, J. Harte, A. Hastings, P. A. Marquet, N. D. Martinez, A. Mooers, P. Roopnarine, G. Vermij, J. W. Williams, R. Gillespie, J. Kitzes, C. Marshall, N. Matzke, D. P. Mindell, E. Revilla, A. B. Smith, Approaching a state shift in Earth's biosphere. *Nature* **486**, 52–58 (2012).

133. H. J. Fowler, G. Lenderink, A. F. Prein, S. Westra, R. P. Allan, N. Ban, R. Barbero, P. Berg, S. Blenkinsop, H. X. Do, S. Guerreiro, J. O. Haerter, E. J. Kendon, E. Lewis, C. Schaer, A. Sharma, G. Villarini, C. Wasko, X. Zhang, Anthropogenic intensification of short-duration rainfall extremes. *Nat. Rev. Earth Environ.* **2**, 107–122 (2021).

134. L. Gudmundsson, J. Boulange, H. X. Do, S. N. Gosling, M. G. Grillakis, A. G. Koutroulis, M. Leonard, J. Liu, N. M. Schmied, L. Papadimitriou, Y. Pokhrel, S. I. Seneviratne, Y. Satoh, W. Thiery, S. Westra, X. Zhang, F. Zhao, Globally observed trends in mean and extreme river flow attributed to climate change. *Science* **371**, 1159–1162 (2021).

135. J. Spinoni, G. Naumann, H. Carrao, P. Barbosa, J. Vogt, World drought frequency, duration, and severity for 1951–2010. *Int. J. Climatol.* **34**, 2792–2804 (2014).

136. T. G. Huntington, Evidence for intensification of the global water cycle: Review and synthesis. *J. Hydrol.* **319**, 83–95 (2006).

137. J. Jägermeyr, A. Pastor, H. Biemans, D. Gerten, Reconciling irrigated food production with environmental flows for sustainable development goals implementation. *Nat. Commun.* **8**, 15900 (2017).

138. A. V. Pastor, F. Ludwig, H. Biemans, H. Hoff, P. Kabat, Accounting for environmental flow requirements in global water assessments. *Hydrol. Earth Syst. Sci.* **18**, 5041–5059 (2014).

139. V. Virkki, E. Alanärä, M. Porkka, L. Ahopelto, T. Gleeson, C. Mohan, L. Wang-Erlandsson, M. Flörke, D. Gerten, S. N. Gosling, N. Hanasaki, H. Müller Schmied, N. Wanders, M. Kummu, Globally widespread and increasing violations of environmental flow envelopes. *Hydrol. Earth Syst. Sci.* **26**, 3315–3336 (2022).

140. P. Greve, B. Orlowsky, B. Mueller, J. Sheffield, M. Reichstein, S. I. Seneviratne, Global assessment of trends in wetting and drying over land. *Nat. Geosci.* **7**, 716–721 (2014).

141. P. Micklin, The aral sea disaster. *Annu. Rev. Earth Planet. Sci.* **35**, 47–72 (2018).

142. W. M. Hammond, A. P. Williams, J. T. Abatzoglou, H. D. Adams, T. Klein, R. López, C. Sáenz-Romero, H. Hartmann, D. D. Breshears, C. D. Allen, Global field observations of tree die-off reveal hotter-drought fingerprint for Earth's forests. *Nat. Commun.* **13**, 1761 (2022).

143. R. S. Cottrell, K. L. Nash, B. S. Halpern, T. A. Remenyi, S. P. Corney, A. Fleming, E. A. Fulton, S. Hornborg, A. Johne, R. A. Watson, J. L. Blanchard, Food production shocks across land and sea. *Nat. Sustain.* **2**, 130–137 (2019).

144. J. Schöngart, F. Wittmann, A. Faria de Resende, C. Assahira, G. de Sousa Lobo, J. R. D. Neves, M. da Rocha, G. B. Mori, A. C. Quaresma, L. O. Demarchi, B. W. Albuquerque, Y. O. Feitosa, G. da Silva Costa, G. V. Feitoza, F. M. Durgante, A. Lopes, S. E. Trumbore, T. S. F. Silva, H. ter Steege, A. L. Val, W. J. Junk, M. T. F. Piedade, The shadow of the Balbina dam: A synthesis of over 35 years of downstream impacts on floodplain forests in Central Amazonia. *Aquat. Conserv. Mar. Freshw. Ecosyst.* **31**, 1117–1135 (2021).

145. B. R. Deemer, J. A. Harrison, S. Li, J. J. Beaulieu, T. DelSontro, N. Barros, J. F. Bezerra-Neto, S. M. Powers, M. A. dos Santos, J. A. Vonk, Greenhouse gas emissions from reservoir water surfaces: A new global synthesis. *BioScience* **66**, 949–964 (2016).

146. A. Clarke, V. Kapustin, Hemispheric aerosol vertical profiles: Anthropogenic impacts on optical depth and cloud nuclei. *Science* **329**, 1488–1492 (2010).

147. P.-A. Monerie, L. J. Wilcox, A. G. Turner, Effects of anthropogenic aerosol and greenhouse gas emissions on northern hemisphere monsoon precipitation: Mechanisms and uncertainty. *J. Clim.* **35**, 2305–2326 (2022).

148. J. Cao, H. Wang, B. Wang, H. Zhao, C. Wang, X. Zhu, Higher sensitivity of northern hemisphere monsoon to anthropogenic aerosol than greenhouse gases. *Geophys. Res. Lett.* **49**, e2022GL100270 (2022).

149. B. Zhuang, Y. Gao, Y. Hu, H. Chen, T. Wang, S. Li, M. Li, M. Xie, Interaction between different mixing aerosol direct effects and East Asian summer monsoon. *Clim. Dyn.* **61**, 1157–1176 (2022).

150. D. M. Westervelt, Y. You, X. Li, M. Ting, D. E. Lee, Y. Ming, Relative importance of greenhouse gases, sulfate, organic carbon, and black carbon aerosol for south asian monsoon rainfall changes. *Geophys. Res. Lett.* **47**, e2020GL088363 (2020).

151. E. D. Galbraith, E. Y. Kwon, A. Gnanadesikan, K. B. Rodgers, S. M. Griffies, D. Bianchi, J. L. Sarmiento, J. P. Dunne, J. Simeon, R. D. Slater, A. T. Wittenberg, I. M. Held, Climate variability and radiocarbon in the CM2Mc Earth system model. *J. Clim.* **24**, 4230–4254 (2011).

152. W. von Bloh, S. Schaphoff, C. Müller, S. Rolinski, K. Waha, S. Zaehle, Implementing the nitrogen cycle into the dynamic global vegetation, hydrology, and crop growth model LPJmL (version 5.0). *Geosci. Model Dev.* **11**, 2789–2812 (2018).

153. P. C. D. Milly, A. B. Shmakin, Global modeling of land water and energy balances. Part I: The land dynamics (LaD) model. *J. Hydrometeorol.* **3**, 283–299 (2002).

154. J. L. Anderson, V. Balaji, A. J. Broccoli, W. F. Cooke, T. L. Delworth, K. W. Dixon, L. J. Donner, K. A. Dunne, S. M. Freidenreich, S. T. Garner, R. G. Gudgel, C. T. Gordon, I. M. Held, R. S. Hemler, L. W. Horowitz, S. A. Klein, T. R. Knutson, P. J. Kushner, A. R. Langenhost, N. C. Lau, Z. Liang, S. L. Malyshev, P. C. D. Milly, M. J. Nath, J. J. Ploshay, V. Ramaswamy, M. D. Schwarzkopf, E. Shevliakova, J. J. Sirutis, B. J. Soden, W. F. Stern, L. A. Thompson, R. J. Wilson, A. T. Wittenberg, B. L. Wyman, The new GFDL global atmosphere and land model AM2-LM2: Evaluationvwith prescribed SST simulations. *J. Clim.* **17**, 4641–4673 (2004).

155. S. Sitch, B. Smith, I. C. Prentice, A. Arneth, A. Bondeau, W. Cramer, J. O. Kaplan, S. Levis, W. Lucht, M. T. Sykes, K. Thonicke, S. Venevsky, Evaluation of ecosystem dynamics, plant geography and terrestrial carbon cycling in the LPJ dynamic global vegetation model. *Glob. Change Biol.* **9**, 161–185 (2003).

156. D. Gerten, S. Schaphoff, U. Haberlandt, W. Lucht, S. Sitch, Terrestrial vegetation and large-scale water balance. Hydrological evaluation of a dynamic global vegetation model. *J. Hydrol.* **286**, 249–270 (2004).

157. A. Bondeau, P. Smith, S. Zaehle, S. Schaphoff, W. Lucht, W. Cramer, D. Gerten, H. Lotze-Campen, C. Müller, M. Reichstein, B. Smith, Modelling the role of agriculture for the 20th century global terrestrial carbon balance. *Glob. Change Biol.* **13**, 1–28 (2007).

158. K. Thonicke, A. Spessa, I. C. Prentice, S. P. Harrison, L. Dong, C. Carmona-Moreno. The influence of vegetation, fire spread and fire behaviour on biomass burning and trace gas emissions: Results from a process-based model. *Biogeosci.* **7**, 1991–2011 (2010).

159. M. Drüke, M. Forkel, W. von Bloh, B. Sakschewski, M. Cardoso, M. Bustamante, J. Kurths, K. Thonicke. Improving the LPJmL4-SPITFIRE vegetation-fire model for South America using satellite data. *Geosci. Model. Dev.* **12**, 5029–2054 (2019).

160. M. Forkel, N. Carvalhais, S. Schaphoff, W. von Bloh, M. Migliavacca, M. Thurner, K. Thonicke, Identifying environmental controls on vegetation greeness phenology through model-data integration. *Biogeosci.* **11**, 7025–7050 (2014).

161. M. Forkel, M. Drüke, M. Thurner, W. Dorigo, S. Schaphoff, K. Thonicke, W. von Bloh, N. Carvalhais, Constraining modelled global vegetation dynamics and carbon turnover using multiple satellite observations. *Sci. Rep.* **9**, 18757 (2019).

162. Fader, S. Rost, C. Müller, A. Bondeau, D. Gerten, virtual water content of temperate cereals and maize: Present and potential future patterns. *J. Hydrol.* **384**, 218–231 (2010).

163. V. Kattsov, R. Federation, C. Reason, S. Africa, A. A. Uk, T. A. Uk, J. Baehr, A. B. Uk, J. Catto, J. S. Canada, A. S. Uk, *Evaluation of climate models (AR5), Climate Change 2013 - The Physical Science Basis* (Cambridge University Press, 2013), pp. 741–866.

164. M. Santoro, O. Cartus, S. Mermoz, A. Bouvet, T. Le Toan, N. Carvalhais, D. Rozendaal, M. Herold, V. Avitabile, S. Quegan, J. Carreiras, Y. Rauste, H. Balzter, C. C. Schmullius, F. M. Seifert, A detailed portrait of the forest aboveground biomass pool for the year 2010 obtained from multiple

remote sensing observations. *Geophys. Res. Abstr.* **20**, EGU2018-18932 (2018). https://meetingorganizer.copernicus.org/EGU2018/EGU2018-18932.pdf

165. P. Gkatsopoulos, A methodology for calculating cooling from vegetation evapotranspiration for use in urban space microclimate simulations. *Proc. Environ. Sci.* **38**, 477–484 (2017).

166. N. Unger, Human land-use-driven reduction of forest volatiles cools global climate. *Nat. Clim. Change* **4**, 907–910 (2014).

167. W. A. Hoffmann, R. B. Jackson, Vegetation-climate feedbacks in the conversion of tropical savanna to grassland. *J. Clim.* **13**, 1593–1602 (2000).